

Mass loss from dwarf spheroidal galaxies: the origins of shallow dark matter cores and exponential surface brightness profiles

J. I. Read and G. Gilmore

Institute of Astronomy, Cambridge University, Madingley Road, Cambridge, CB3 0HA

Accepted. Received; in original form

ABSTRACT

Dwarf spheroidal galaxies have shallow central dark matter density profiles, low angular momentum and approximately exponential surface brightness distributions. Through N-body simulations and analytic calculations we investigate the extent to which these properties can be generated from “typical” Λ CDM galaxies, which differ in all of these properties, by the dynamical consequences of feedback.

We find that, for a wide range of initial conditions, one impulsive mass loss event will naturally produce a surface brightness profile in the remaining stellar component of a dwarf spheroidal galaxy (dSph) which is well fit over many scale lengths by an exponential, in good qualitative agreement with observations of Local Group dSphs. Furthermore, two impulsive mass loss phases, punctuated by significant gas re-accretion, are found to be sufficient to transform a central density cusp in the dark matter profile into a near-constant density core. This may then provide the missing link between current cosmological simulations, which predict a central cusp in the dark matter density profile, and current observations, which find much shallower central density profiles.

We also look at the angular momentum history of dSphs and demonstrate that if these galaxies have spent most of their lifetime in tidal isolation from massive galaxies then they cannot have formed from high angular momentum gas discs.

Key words:

1 INTRODUCTION

Over recent years, dwarf galaxies have become increasingly interesting objects in the light of hierarchical formation models. In the current Λ CDM paradigm, all structure in the universe forms from the successive mergers of smaller substructures (see e.g. White & Rees (1978), Navarro et al. (1996b), Subramanian et al. (2000), Dekel et al. (2003), Governato et al. (2004); or for a review Steinmetz (1999)). In this scenario, low mass dwarf galaxies may be the left-over remnants of the hierarchical merging process. If this is the case, then their stellar populations should be able to tell us much about merger histories (Tolstoy et al., 2003); their internal angular momentum and surface brightness profiles should contain vital clues as to the coupling of the gas to the dark matter in the early universe (van den Bosch et al., 2001); and their underlying dark matter distribution, largely unaffected by merging, should be able to tell us much about the detailed nature of dark matter (Kleyna et al., 2001).

The dwarf galaxies of the Local Group can be split into three broad categories: dwarf irregular galaxies (dIrr), which are rich in HI gas, transition galaxies (dIrr/dSph), which contain some HI gas and dwarf spheroidal galaxies (dSph), which contain little or no HI gas (Mateo (1998), van den Bergh (1999), Ferguson & Binggeli (1994) and Grebel (1999)). The dSph galaxies have surface bright-

ness profiles which are well fit by an exponential over many scale lengths (Walcher et al. (2003) and Odenkirchen et al. (2001)) and there is mounting evidence that many of the Local Group dwarfs have very little internal angular momentum (Kleyna et al. (2001) and Mateo (1998)). Finally, while little is known in general about the distribution of dark matter in these galaxies, one recent indirect measurement suggests that Ursa Minor (UMi) has a central, constant density, dark matter core (Kleyna et al., 2003), similar to those observed in LSB galaxies (see e.g. de Blok et al. (2001)).

In contrast to these observations, if the dwarf galaxies of the Local Group are indeed the untouched remnants of a hierarchical merging process, then current numerical simulations predict a wide range of angular momenta for these galaxies (see e.g. Bullock et al. (2001) and Colin et al. (2003)), while their central dark matter density distribution should exhibit a log-slope of $1 < \alpha < 1.5$ (see e.g. Klypin et al. (2001), Ghigna et al. (2000) and Navarro et al. (1996b)).

These differences between the numerical experiments and the observations could be an indication that the current cosmological paradigm breaks down on small scales; or it could be a result of a complex evolutionary history for the Local Group dwarfs due to some form of *feedback*. The evidence for a complex evolution is compelling: gas poor dSph galaxies are found preferentially close to their host galaxy while gas rich dIrr lie further away, indicating

arXiv:astro-ph/0409565v1 23 Sep 2004

an environmental dependence for the galaxy morphology (Mateo (1998), Grebel et al. (2003) and van den Bergh (1999)); the star formation histories for the Local Group dSph galaxies are complex and varied (Dolphin (2002), Monelli et al. (2003), Hernandez et al. (2000) and Ikuta & Arimoto (2002)); and the currently very low mass to light ratio, small HI mass, and low chemical abundance in dSph galaxies is suggestive of significant gas mass loss (Mateo (1998), Grebel et al. (2003), Kleyana et al. (2001) and Carigi et al. (2002)).

From a theoretical viewpoint, it has been known for some time that feedback is required within hierarchical clustering theories in order to explain the lack of small scale power in the observed galaxy luminosity function (White & Rees (1978), Benson et al. (2003) and Binney (2004)); while mass loss as a form of feedback has been discussed extensively in the literature, both with regards to large spiral galaxies (see e.g. Silk & Rees (1998)) and smaller dwarf galaxies (see e.g. Larson (1974), Dekel & Silk (1986), Dekel & Woo (2003), Hayashi et al. (2003) and Efstathiou (2000)).

Many mechanisms have been proposed to drive gas mass loss from dwarf galaxies, including ram pressure stripping (Einasto et al. (1974) and Grebel et al. (2003)), supernovae explosions (Larson (1974), Dekel & Silk (1986), Dekel & Woo (2003) and Efstathiou (2000)); photoevaporation (Quinn et al. (1996) and Barkana & Loeb (1999)); and the effects of galaxy harassment and tidal stripping from a large host galaxy (Mayer et al. (2001), Moore et al. (1996), Moore et al. (1998) and Hayashi et al. (2003)). It is likely that all of these mechanisms act in tandem to a greater or lesser extent in the evolution of both dSph and dIrr galaxies.

In this study we consider the dynamical effect of mass loss on the remaining stars and dark matter in isolated dSph galaxies. We simplify the analysis to be purely dynamical, explicitly not considering the physical processes which drive the mass loss. In this way we are able to study the maximum possible dynamical effect on the surviving galaxy, to see if, in principle, extreme mass loss can change the structure of dwarf galaxies.

Other authors have previously studied the dynamical effect of mass loss from dwarf galaxies but focused only on the effects on the remaining dark matter (Navarro et al. (1996a), Gelato & Sommer-Larsen (1999) and Gnedin & Zhao (2002)), or specifically on the hydrodynamics of gas mass loss (Mac Low & Ferrara (1999)).

In this paper we present the first comprehensive dynamical study of mass loss from progenitors to what are currently dSph galaxies, using the fully self consistent 3D N-body code, GADGET (Springel et al., 2001). We perform the highest resolution simulations to date and unlike previous studies we focus both on the response of the dark matter to mass loss *and* the response of the stellar component. This last point is critical since the final surface brightness and angular momentum distribution of the stars in our dynamical models can then be compared with data from the Local Group dSph galaxies.

In doing this we pose the question: can mass loss explain the low angular momentum, exponential surface brightness distribution and cored central dark matter distribution observed in the dSph galaxies of the Local Group?

This paper is organised as follows: In section 2, we present our numerical method for setting up the initial conditions, performing the mass loss and subsequently evolving the system. In section 3, we present the results of a suite of numerical N-body simulations to determine the dynamical response of a two-component galaxy

comprising baryons* and dark matter, initially in equilibrium, to significant baryonic mass loss. This section is divided into three sub-sections, each focusing on a potential observational signature of the remnant galaxy after mass loss. Section 3.1 focuses on the dynamical effect of mass loss on the angular momentum distribution of the baryons, section 3.2 focuses on the dynamical effect of mass loss on the radial density profile of the dark matter and section 3.3 focuses on the surface density profile of the baryons after mass loss. In section 4, we discuss the simulation results in comparison with other results already in the literature and highlight, clarify and justify the choice of assumptions inherent in this work. In section 5, we then go on to compare the results of the simulations with observations of dwarf galaxies from the Local Group. Finally, in section 6, we present our conclusions.

2 THE NUMERICAL METHOD

In this section we describe the methodology and initial conditions for a suite of simulations which track the dynamical response of a two component system of baryons and dark matter to significant baryon mass loss.

2.1 The initial conditions

We used a two-component model for the initial conditions comprising some baryons and some dark matter. The system was set up in equilibrium as in Hernquist (1993). The density profiles were populated with particles using Monte Carlo methods, and the velocity structure was then realised using moments of the Collisionless Boltzmann Equation, assuming a Maxwellian distribution (see Hernquist (1993) for more detail).

A recent paper by Kazantzidis et al. (2004) has suggested that the Maxwellian velocity approximation used by Hernquist (1993) in setting up the initial conditions can lead to spurious results for simulations performed over long timescales. To test that the results presented here are not affected by the Maxwellian approximation we re-simulated one run using an initial condition generator which drew the velocities directly from a numerically calculated distribution function, as in Kazantzidis et al. (2004). The results showed excellent agreement with the runs performed using the Maxwellian approximation for the initial conditions.

We used two different density profiles for the baryons and two for the dark matter in order to cover the extrema initial conditions of interest. For the baryons, we considered a rotating exponential disc or a generalised Hernquist spheroid, which may be set rotating if required[†](see Hernquist (1990), Saha (1992) and Zhao (1996)). These two profiles are relevant since an exponential disc may be morphologically close to the dIrr of the Local Group at the present epoch, while a spheroidal profile is close to the dSph galaxies of the Local Group observed at the current epoch (Mateo (1998), Grebel (1999) and van den Bergh (1999)). For the dark matter, we used one of two profiles - the Hernquist profile, or the truncated isothermal sphere (Hernquist, 1993). The Hernquist profile is relevant since in the central regions it closely resembles the profiles found in large

* We refer throughout this paper to the gas and stars collectively as baryons. This is because we do not include any gas hydrodynamics in our models, and so the gas and stars are dynamically indistinguishable.

[†] As discussed in Hernquist (1993), the rotating spheroids start with systematically less angular momentum than the rotationally supported discs.

N-body numerical simulations of dark matter structure formation (see e.g. (Navarro et al., 1996b) and Ghigna et al. (2000)). The truncated isothermal sphere profile is relevant since it provides a good fit to the dark matter density profiles derived from real data (see e.g. Borriello & Salucci (2001) and de Blok et al. (2001)). The analytic forms for these profiles are summarised for completeness below:

The exponential disc is given by:

$$\rho_d(R, z) = \frac{M_d}{4\pi h_d^2 z_0} \exp(-R/h_d) \text{sech}^2\left(\frac{z}{z_0}\right) \quad (1)$$

where R and z are the familiar cylindrical coordinates, h_d is the disc scale length, z_0 is the disc scale height and M_d is the disc mass.

The generalised Hernquist profile is given by (see e.g. Hernquist (1990), Saha (1992) and Zhao (1996)):

$$\rho_{b,i}(r) = \frac{C(\alpha, \beta, \gamma)}{\left(\frac{r}{h_b}\right)^\alpha \left(1 + \left(\frac{r}{h_b}\right)^\gamma\right)^{\frac{\beta-\alpha}{\gamma}}} \quad (2)$$

Where $C(\alpha, \beta, \gamma)$ is a normalisation constant, h_b is the baryon scale length, α is the power law log-slope of the baryons interior to h_b , β is the log-slope exterior to h_b and γ controls the smoothness of the transition at h_b .

The Hernquist profile is given by (c.f. equation 2 with $\alpha = 1$, $\beta = 4$ and $\gamma = 1$):

$$\rho_h(r) = \frac{M_h}{2\pi a_h^3} \frac{1}{r/a_h(1+r/a_h)^3} \quad (3)$$

where M_h is the mass of the halo, and a_h is the scale length. The truncated isothermal sphere is given by:

$$\rho_h(r) = \frac{M_h}{2\pi^{3/2}} \frac{\zeta \exp(r^2/r_t^2)}{r_t (r^2 + r_c^2)} \quad (4)$$

$$\zeta = \left(1 - \sqrt{\pi} q \exp(q^2) (1 - \text{erf}(q))\right)^{-1}$$

where M_h is the halo mass, r_t is the tidal cut-off radius, r_c is the core radius and $q = r_c/r_t$.

For some of the runs we model a dissipation and collapse phase for the baryons. For these runs the baryon collapse was modelled either numerically, by slowly increasing the mass of the baryons over the contraction time, t_{cont} , while holding the baryons fixed (c.f. Gelato & Sommer-Larsen (1999) and Jesseit et al. (2002)), or analytically using a similar prescription to that set out in Gnedin & Zhao (2002) (see appendix A). For the numerical baryon contraction, the system was then evolved for a further 30 time units before mass loss to ensure equilibrium; the results were found not to be sensitive to this parameter.

2.2 Units

For all of the simulations discussed subsequently, we use a system of units such that $G = M_{d,b} = h_{d,b} = 1$, where $M_{d,b}$ is the mass of the baryons (disc or spheroid), $h_{d,b}$ is the scale length of the baryons and G is the gravitational constant. For initial conditions which approximate a typical dIrr galaxy, $M_{d,b} \sim 10^8 M_\odot$ and $h_{d,b} \sim 1 \text{ kpc}$. Unit time is then 4.7×10^7 years, while unit velocity is 20.7 km s^{-1} . From here on, we will leave the results in simulation units so that they can be scaled for comparison with a range of systems.

2.3 Equilibrium tests and resolution issues

As with any simulation, it is important to assess which aspects of the simulation can be viewed as physical and which are a product of finite resolution and computational techniques. As such, we have been careful to test the code using a wide range of softening parameters and particle numbers. Equilibrium tests were carried out on every run for 15 time units to ensure that the system remained unchanged before any mass was removed. Most runs were carried out with 15,000 disc and 150,000 halo particles and with disc and halo softening parameters of 0.04 and 0.02 respectively. The softening parameters were chosen using the analytic criteria of Power et al. (2003). Test runs with lower softening parameters were compared with the standard runs and no changes were observed. Finally, key runs were re-simulated at higher resolution with 68,181 disc and 681,818 halo particles with softening parameters of 0.02 and 0.011 respectively, to test for convergence; excellent agreement was found with the lower resolution runs.

Poisson noise was found to set in at less than 0.1 baryon scale lengths for all of the simulations, indicating that all simulations were well resolved over the scales of interest for this study.

The N-body numerical calculations were performed using the GADGET tree code (Springel et al. (2001)). The GADGET code is particularly advantageous for this study because:

1. It allows for variable time steps for each particle and hence provides excellent time resolution at small radii where we are most interested in the halo density profile.
2. It comes in a massively parallel distribution which scales very efficiently with particle number, allowing us to re-simulate the most interesting runs at high resolution.

The GADGET code was found to conserve energy to better than one part in 10^5 over the typical simulation time of 15 time units.

As a further test of the GADGET code, we re-simulated one run using a different Poisson integrator described in Dehnen (2000). For this run, we used fixed time steps and evolved the particles with a standard leap-frog algorithm (see e.g. Barnes & Hut (1986)). We found excellent agreement with the results from GADGET.

Finally, for a collisionless system, it is important that two-body relaxation is negligible over the entire simulation time (Binney & Tremaine (1987) and Power et al. (2003)). For all of the runs, two body relaxation became important only interior to ~ 2 halo softening lengths over the longest simulation times of 100 units ($\sim 7 \text{ Gyrs}$).

2.4 Mass loss and system evolution

We removed the baryonic mass by adding a large velocity vector of random direction to some of the baryons such that a fraction of them were removed over a given time period and from a particular region of the initial disc or spheroid. The response due to this mass loss was then tracked using the GADGET tree code (see section 2.3 and Springel et al. (2001)).

It is important to note explicitly that there is *no gas physics* in our model; we wish to model the *dynamical effects* of mass loss, not the hydrodynamics involved in actually performing gas mass removal.

After mass loss most runs were evolved for a further 15 time units ($\sim 1 \text{ Gyr}$). Two key runs were evolved for a longer time of 100

units (~ 7 Gyrs) to test for equilibrium. Given that the typical orbital times of Local Group dSph galaxies around the Milky Way are $\sim 1 - 2$ Gyrs (Dinescu et al. (2004), Piatek et al. (2002), Schweitzer & Cudworth (1996) and Schweitzer et al. (1995)), we do not generally consider the long-time evolution of the models presented here since it is likely that, over these longer times, tidal effects become important. The longer-time evolution of these dynamical models, including the effects of tides, will be the subject of future work.

3 RESULTS

In this section we describe the results from a suite of simulations which track the dynamical response of a two-component system comprising baryons and dark matter, initially in equilibrium, to significant baryon mass loss. The results are divided into three subsections, each focusing on a potential observational signature of the remnant galaxy after mass loss. Section 3.1 focuses on the dynamical effect of mass loss on the angular momentum distribution of the baryons, section 3.2 focuses on the dynamical effect of mass loss on the radial density profile of the dark matter and section 3.3 focuses on the surface density profile of the baryons after mass loss. In all cases comparisons with real data are deferred until section 5.

The simulations are labelled in order of discussion from A through to C. The particle number, force softening, mass loss parameters and initial condition density and velocity profile parameters are given in table 1. Some animations, illustrating the simulations in action can be viewed at:

www.ast.cam.ac.uk/~jir22

3.1 Angular momentum

In this section we consider the dynamical effect of mass loss from two-component galaxies, initially in equilibrium, on the final angular momentum distribution of the baryons. In doing this we seek to find out whether or not mass loss can reconcile the observed, low angular momenta of the Local Group dSph galaxies with the wide range of angular momenta predicted by cosmological simulations (see section 1).

We consider first a set of extreme models where 95% of the initial baryonic mass is removed on a disc crossing time - the impulsive mass loss case. These extreme models are relevant since, if they fail to appreciably perturb the initial angular momentum distribution, then we can rule out a wide range of more reasonable mass loss scenarios. 95% mass loss is also a reasonable place to start since, if dwarf galaxies formed with the cosmological mean baryon fraction, then they must have lost $\sim 95\%$ of their baryonic mass by the present epoch (Spergel et al. (2003) and Kleyna et al. (2001)).

The simulations are labelled, in order of discussion, from A1 through to A8. The initial conditions and model parameters for all of the runs are summarised in table 1.

3.1.1 Quantifying the angular momentum of a remnant galaxy

While in these simulations we are able to measure exactly the angular momentum distribution of the baryons after mass loss, this is not the case for real dwarf galaxies observed in projection on the sky. As such, it is also useful to have a statistical measure of the observable amount of angular momentum.

To quantify the measurable amount of angular momentum left

in a remnant system, we performed 500 random realisations of a non-rotating spheroid with the same velocity dispersion as used for the rotating spheroid initial conditions, but with only 750 baryon particles to mimic the effect of a 95% mass loss. We then define the *rotation factor*, RF , as:

$$RF = ||\bar{v}_l - \bar{v}_r| - |\bar{v}_t - \bar{v}_b|| \quad (5)$$

where \bar{v}_i ($i = l, r, t, b$) are the average projected velocities over the left, right, top and bottom sections of the velocity projection, rotated so that the maximal rotation axis is vertical and centred.

For the non-rotating spheroid, the mean rotation factor was 0.01, while the 3σ deviation from the mean was 0.08. We define, then, a system with *statistically significant* rotation as one which has $RF > 0.08$ - i.e. with a rotation factor which is greater than 3σ from the mean for a non-rotating system. For comparison, the rotation factors for initial conditions where the baryons were set up in a rotating disc or rotating spheroid were 0.64 and 0.36 respectively.

3.1.2 Random mass removal - runs A1-A6

The first case of interest is that where the mass was removed from randomly selected regions of the baryon spatial distribution. In the following simulation runs A1-A6, 95% of the mass of the baryons was removed in one baryon crossing time (~ 1 in simulation units). In runs A1-A3 the baryons were initially set up in equilibrium with a rotating exponential disc with $M_b = 1, h_d = 1$ and $z_0 = 0.2$. A Toomre Q-parameter of 1.5 was used, corresponding to an initially stable disc (Binney & Tremaine, 1987), although changes to this parameter were not found to significantly affect the results. From run A1 through to A3 all that was changed in the initial conditions was the underlying dark matter profile, with the mass of dark matter interior to the baryons decreasing from A1 to A3. Similarly, runs A4-A6 had the same decreasing sequence of dark matter mass, but the baryons were initially set up in equilibrium with a rotating Hernquist density profile of mass, $M_b = 1$, and scale length, $h_b = 1$. For these runs the initial angular momentum was less than in the disc cases as discussed in section 2.1. The initial conditions for all of the runs are summarised in table 1.

Figure 1 displays the specific angular momentum of the baryons before (dotted lines) and after mass loss (solid lines) for runs A1-A8. Notice that, as the initial dark matter mass interior to the baryons decreases from run A1 to A3, the decrease in angular momentum is greater. The same trend is observed in runs A4 to A6.

The rotation factors, marked in the bottom left corner of each plot, follow the same trend as discussed above for the baryon specific angular momentum after mass loss. Only one run (A6) falls below statistically significant rotation at the 3σ level after mass loss. This run represents the most extreme model where the baryons are initially, largely pressure supported ($v_r/\sigma = 0.8^\ddagger$) and where the initial dark matter mass interior to the baryons is very low ($\sim 1\%$ of the initial baryon mass).

\ddagger In this context v_r is the rotational velocity of the baryons at the edge of the light distribution, while σ is the mean velocity dispersion averaged over the whole distribution. v_r is averaged over a radial slice of thickness 0.5 in simulation units and at an outer radius, r_l , where v_r is maximised. We do not allow the particle number at r_l to fall below order 10 so as to avoid sampling at large radii where statistical noise from low particle numbers can

Run	N_b	ϵ_b	N_{dm}	ϵ_{dm}	t_{cont}	Baryon Profile	Halo Profile	δ	t_{ml}
A1	68,181	0.02	681,818	0.011	0	D,1,1,0.2,R	H,10,10	0.95	1
A2	15,000	0.04	150,000	0.02	0	D,1,1,0.2,R	H,2,10	0.95	1
A3	15,000	0.04	150,000	0.02	0	D,1,1,0.2,R	T,10,40,10	0.95	1
A4	68,181	0.02	681,818	0.011	0	S,1,4,1,R	H,10,10	0.95	1
A5	15,000	0.04	150,000	0.02	0	S,1,4,1,R	H,2,10	0.95	1
A6	15,000	0.04	150,000	0.02	0	S,1,4,1,R	T,10,40,10	0.95	1
A7	68,181	0.02	681,818	0.011	0	D,1,1,0.2,R	H,10,10	0.99	1
A8	68,181	0.02	681,818	0.011	0	S,1,4,1,R	H,10,10	0.97	1
					(a)1				
B1	15,000	0.04	150,000	0.02	(b)15	S,1,4,1	H,10,10	0.95	1
					(c) ∞				
					(a)15				
B2	68,181	0.02	681,818	0.011	(b)40	S,1,4,1	H,10,50	0.95	1
					(c) ∞				
					(a)15				
B3	15,000	0.04	150,000	0.02	(b) ∞	S,1,4,1	H,2,10	0.95	1
B4	68,181	0.02	681,818	0.011	*	S,1,4,1	H,5,10	0.95	1
C1	68,181	0.02	681,818	0.011	0	S,1,4,1	H,10,10	0.95	1
C2	15,000	0.04	150,000	0.02	0	S,0,3,1	H,2,10	0.95	1
C3	15,000	0.04	150,000	0.02	0	S,1,4,1	Fix H,10,10	0.95	1
C4	15,000	0.04	150,000	0.02	∞	S,1,4,1	H,10,10	0.95	1
C5	15,000	0.04	150,000	0.02	0	S,1,4,1	H,10,10	0.95	9

Table 1. Initial conditions for simulation runs A-C. The table columns from left to right are: the run label, the number of baryon particles, N_b , the baryon force softening, ϵ_b , the number of dark matter particles, N_{dm} , the dark matter force softening, ϵ_{dm} , the baryon infall time, t_{cont} , the baryon radial density profile, the halo radial density profile, the baryon mass loss fraction, δ , and finally, the baryon outflow time, t_{ml} . Where the dark matter was not allowed to contract in response to the addition of the baryons, $t_{cont} = 0$, and where the contraction was set up analytically for the initial conditions (the true adiabatic case), $t_{cont} = \infty$ (see appendix A for more details). The notation used for the baryon density profile is: D, M_b , h_d , z_0 ,R for an exponential disc of mass, M_b , scale length, h_d , and scale height, z_0 , which is [R]otationally supported (see equation 1) and: S, α , β , γ ,[R] for a generalised Hernquist spheroid with inner log-density slope, α , outer slope β , transition smoothing, γ , mass $M_b = 1$ and potentially set in [R]otation initially (see equation 2). The notation used for the halo density profile is: H, M_h , a_h for a Hernquist spheroid of mass, M_h , and scale length, a_h , (see equation 3) and T, M_h , r_t , r_c for a truncated isothermal sphere of mass M_h , tidal radius, r_t and core size r_c (see equation 4). For run C3, the halo was held fixed throughout the mass loss and not allowed to respond. The runs A1-A8 are all concerned with the effects of mass loss on the angular momentum profile of the baryons. B1-B4 are concerned with the effects of mass loss on the underlying dark matter distribution and C1-C5 are concerned with the effects of mass loss on the baryon surface density profile and velocity structure. The * next to run B4 for the infall time indicates that this is a special run in which three slow inflow phases over 15 time units were punctuated by phases of fast mass loss over 1 time unit. The system was evolved for 30 time units (~ 2 Gyrs) in-between each mass inflow and each mass outflow phase.

3.1.3 Biased mass removal - runs A6-A8

While the spatially-random mass removal cases do reduce the angular momentum of the progenitor galaxy, in nearly all of the above scenarios significant angular momentum remains in the baryons after mass loss. However, for both the disc and spheroid initial conditions, the majority of the angular momentum is contained at large radii (see figure 1). While not linked to a specific physical model of dSph star-formation and feedback, it is interesting to consider the case of biased mass loss, where mass is lost preferentially from the outer parts of the disc or spheroid. In this way, we preferentially remove the high angular momentum material. This scenario could be of importance for models where material (stellar, gas and dark matter) is tidally stripped from the outer regions through interactions with a massive host galaxy (see e.g. Mayer et al. (2001), Maller & Dekel (2002), Mateo (1998) and section 1).

Figure 1 runs A7 and A8 shows the effect of the removal of all of the mass from the disc and spheroid respectively at radii larger than the disc scale height. This amounts to a mass loss of 99%

lead to spurious results. For the non-rotating spheroid discussed in 3.1.1, $v_r/\sigma = 0.04$.

for the disc (run A7) and 97% for the spheroid (run A8) and should remove all the high angular momentum parts, while leaving a small, approximately spherical, remnant behind.

As can be seen, this biased mass removal has largely worked as one would expect. Much of the angular momentum of the baryons has been removed, while the rotation factors for the remnants (as defined in section 3.1.1) are reduced to 0.12 for both the disc and spheroid cases. However, even in this extreme case, in both runs A7 and A8 statistically significant rotation remains in the remnant galaxies after mass loss. The relevance of these results will be discussed further in section 5.

3.1.4 Asymmetric mass loss

All of the mass loss scenarios considered above far have been spherically symmetric. For tidal stripping, however, or other possible mechanisms of mass loss linked to local star formation rates, the assumption of spherical symmetry could be very poor. As such, we also considered the effects of asymmetric mass loss. The results from these runs were found not to significantly differ in terms of angular momentum loss from those presented above: angular momentum is still difficult to remove through mass loss.

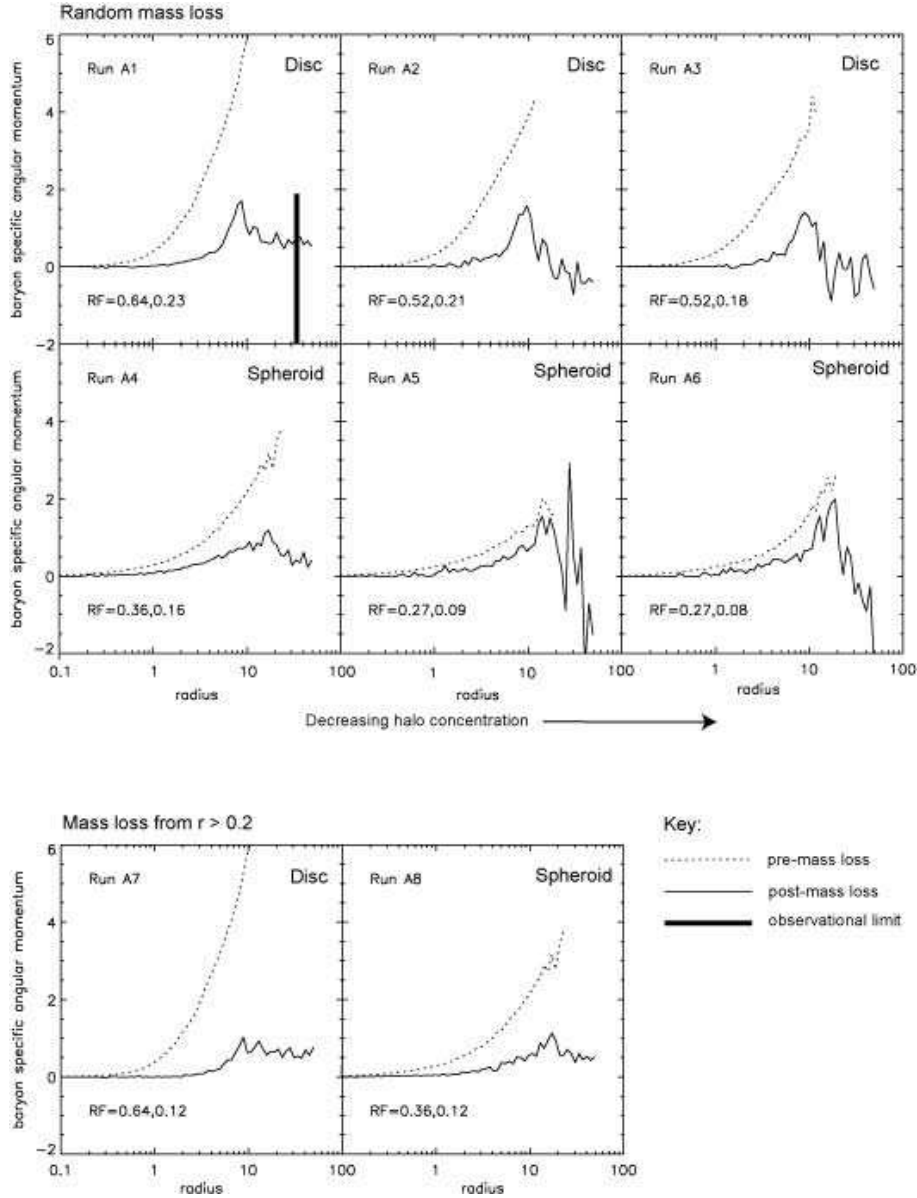


Figure 1. Baryon specific angular momentum profiles before (dotted lines) and after mass loss (solid lines) for runs A1–A8. The initial conditions were as in table 1. The units for all of the runs were as in section 2.2. Marked in the bottom left corner of each run is the rotation factor (see equation 5) before (left of comma) and after (right of comma) the mass loss. A rotation factor of > 0.08 represents statistically significant rotation at the $> 3\sigma$ level. The top six plots (runs A1–A6) show the effect of random mass loss for different initial conditions. From left to right, the dark matter halo concentration is reduced for disc (top) and spheroid (bottom) initial conditions. The bottom two plots (runs A7 and A8) show the effect of removing the mass from all radii larger than 0.2 baryon scale lengths for disc (left) and spheroid (right) initial conditions. Marked on run A1 is the current observational limit, which is the same for all of the runs, where the surface brightness drops below the background noise. Notice that this limit lies beyond the peak in the specific angular momentum after mass loss in all cases.

3.2 The dark matter density profile

In this section we consider the dynamical effect of mass loss from two-component galaxies, initially in equilibrium, on the underlying dark matter distribution. Recall from section 1 that the UMi dSph galaxy appears to have a near-constant central dark matter density profile, whereas cosmological simulations predict a central log slope for the density profile of $1 < \alpha < 1.5$. Here we consider whether or not mass loss could explain this discrepancy.

For brevity we present the results from five simulations involving different extrema initial conditions, labelled B1 through to

B4. A summary of the initial conditions and model parameters for all of the runs is displayed in table 1.

Overlaid on the simulation results are also analytic calculations for the adiabatic response of the halo to baryon dissipation and collapse and the subsequent response of the halo to an impulsive mass loss from the baryons. These calculations are very similar to those presented in Gnedin & Zhao (2002) and are outlined for completeness in appendix A. The analytic calculations are useful for two reasons: they provide an independent check that the numerical code is producing sensible results, and they highlight the important

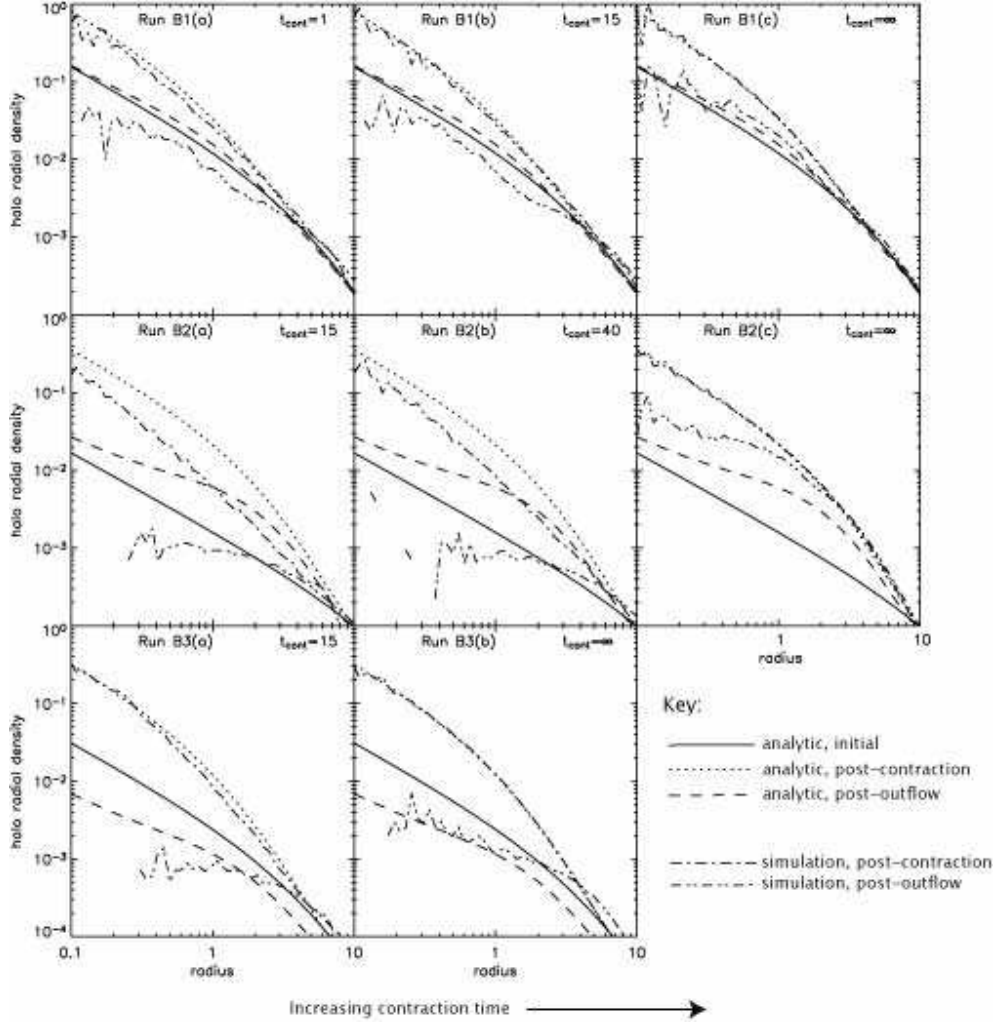


Figure 2. Runs B1–B3: Response of a centrally cusped dark matter halo to the slow addition and fast removal of some baryons. The units for the plot are as in section 2.2. The initial conditions for each run were as in table 1. Run B1 had initial conditions close to the cosmological mean. Runs B2 and B3 were identical to run B1 but with long scale length and low mass dark matter halos respectively. The baryon infall time, t_{cont} , for each run is marked in the top right corner and is increasing from left to right. Where $t_{cont} = \infty$, the contraction of the halo due to the slow addition of the baryons was calculated analytically as in appendix A. The dot-dashed lines show the halo density after the baryons have been added to the system over a time, t_{cont} , while the double-dot dashed lines show the halo density after a subsequent impulsive mass loss over 1 time unit (~ 1 baryon crossing time). The solid lines show the initial halo density profile, the dotted lines show the analytic prediction for the halo density profile for adiabatic mass inflow and the dashed lines show the heuristic analytic prediction for the final halo density profile after mass loss as derived in appendix A. All of the runs were evolved for 15 time units (~ 1 Gyr) after mass loss. Notice that as the inflow time is increased, the contraction of the dark matter halo due to the addition of the baryons (dot-dashed lines) tends towards the adiabatic limit (dotted line). Notice, further that, even when the non-adiabatic inflow cases ($t_{cont} \neq \infty$) produce contracted density profiles which are very close to the adiabatic limit, the resulting density profiles after mass loss are much shallower than the true adiabatic case.

physics involved. For slow gas dissipation and infall, angular momentum, mass and orbital structure must be conserved (i.e. those particles initially on circular orbits will remain on circular orbits). For fast impulsive outflow, or faster gas inflow, angular momentum and mass are still conserved (provided the infall is spherically symmetric) but an initially circular orbit will become a more energetic (more radial) orbit. It is this structural change which leads to an altered density profile in the dark matter after mass loss.

3.2.1 The choice of inflow time

For all of the runs presented in this section we allowed the dark matter halo to contract in response to the addition of the baryons,

either by slowing increasing the mass of the baryons over a time, t_{cont} , while holding the baryons fixed; or by using an analytic prescription for adiabatic mass inflow (see appendix A). We then allowed the system to evolve for a further 30 time units before any mass was removed; the results were found not to be sensitive to this parameter.

To see why it is important to consider a range of inflow timescales for the baryons, it is worth considering the free fall time, t_{ff} , for a pressureless gas sphere of uniform density, $\bar{\rho}$. This is given by (Binney & Tremaine, 1987):

$$t_{ff} = \sqrt{\frac{3\pi}{32G\bar{\rho}}} \quad (6)$$

In simulation units, for typical initial conditions with $M_h = a_h = 10$, this gives $t_{ff} \sim 11$.

We can gain a crude handle on how close to the adiabatic regime the gas inflow is by comparing this gas inflow time with the crossing time for a dark matter particle at the baryon scale length, $t_{cross}(h_b)$. This gives (Binney & Tremaine, 1987):

$$t_{cross}(h_b) = \sqrt{\frac{h_b}{G} \left(\frac{M_h}{(h_b + a_h)^2} + \frac{M_b}{4h_b^2} \right)^{-1}} \quad (7)$$

During the mass inflow phase, we can then find an *upper bound* for t_{cross} by assuming that $M_b = 0$ throughout the contraction.

For $t_{cont} \gg t_{cross}(h_b)$, we should achieve close to adiabatic behaviour. Notice that for $M_h = 10$ and $a_h = 10$, $t_{cross}(h_b) \sim 4$ units. Thus, even gas inflow on a free fall timescale may be non-adiabatic. Faster gas inflow due to, for example, mergers (Naab & Burkert, 2001) or interactions (Mihos & Hernquist, 1994) will then be even further away from the adiabatic limit, and so it is important to consider the case of non-adiabatic inflow.

For most of the runs, we will use $t_{cont} = 15$ units, which translates to $t_{cont} \sim 0.7 \times 10^9$ years - of order a giga-year, for a $10^8 M_\odot$ galaxy with scale length 1kpc (see section 2.2).

3.2.2 The effect of varying the inflow time - run B1

Run B1 (see figure 2) had initial conditions set up as in table 1: $M_h = 10$, $a_h = 10$, $t_{mt} = 1$ and $\delta = 0.95$. This gave a baryon fraction, $f_b = \frac{M_b}{M_b + M_h} = 0.1$ initially and $f_b = 200$ after the mass loss. The three plots B1(a), B1(b) and B1(c) show the effect of varying the baryon infall time, t_{cont} , which is marked on each. For plot B1(c), where $t_{cont} = \infty$, the contraction of the halo due to the slow addition of the baryons was calculated analytically as in appendix A. For all three plots, the dot-dashed lines show the halo density after the baryons have been added to the system over a time, t_{cont} , while the double-dot dashed lines show the halo density after a subsequent impulsive mass loss over 1 time unit (~ 1 baryon crossing time). The solid line shows the initial halo density profile, the dotted line shows the analytic prediction for the halo density profile after adiabatic mass inflow and the dashed line shows the heuristic analytic prediction for the final halo density profile after mass loss as derived in appendix A. Notice that there is a small core interior to ~ 0.2 baryon scale lengths due to particle noise and two-body relaxation (see section 2.3) which can be seen in all of the simulations. This effectively sets the simulation resolution.

Although in all of the runs the contracted halo density profile seems very close to the adiabatic limit (see the double-dot dashed line as compared with the dotted line), the post-mass loss density profiles are quite different (compare the dot-dashed lines in plots B1(a)-B1(c)). For the true adiabatic run, B1(c), the final halo density profile after mass loss is in reasonable agreement with the heuristic analytic prediction from appendix A (see double-dot dashed lines as compared with the dashed line). However, for the faster inflow time runs, the final density profile after mass loss is much shallower. The reason for this is that non-adiabatic inflow (that is inflow on a timescale which is short as compared with the halo dynamical time), does not preserve the initial orbital structure. The initially isotropic halo becomes strongly radially anisotropic after mass inflow. This anisotropy then significantly increases the number of halo particles which become unbound after subsequent mass loss and leads to much shallower final halo density profiles (see appendix A).

This is further illustrated by figure 3, which compares the halo

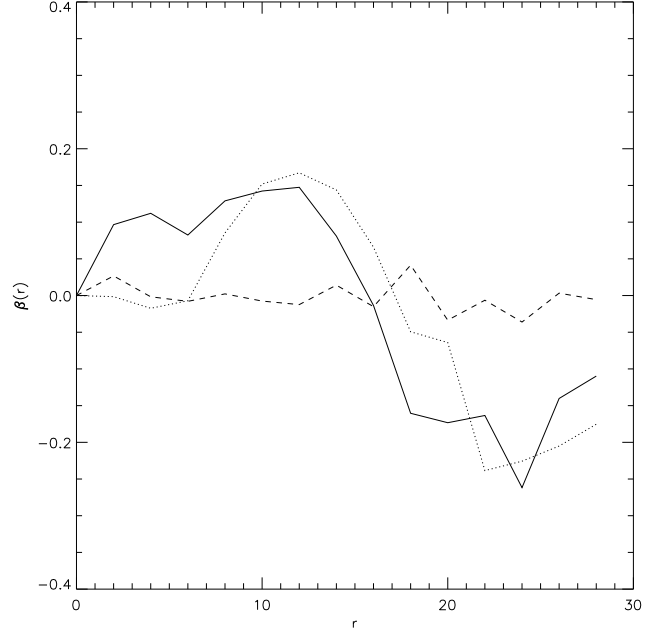


Figure 3. The effect of the baryon inflow time on the halo velocity anisotropy. The lines in the plot show the radially binned halo velocity anisotropy, $\beta(r)$, after mass inflow for run B1. The solid line is for inflow on 1 baryon crossing time (run B1(a)), the dotted line is for inflow over 15 baryon crossing times (run B1(b)) and the dashed line is for the infinitely slow limit of adiabatic inflow, which was set up analytically as in appendix A (run B1(c)). Notice that the amount of anisotropy introduced *increases* as the infall time is *reduced*.

velocity anisotropy, $\beta(r)$, after mass inflow for the different simulation runs B1(a) to B1(c) ($\beta(r) = 1 - \frac{v_\theta^2}{v_r^2}$ is defined as in Binney & Tremaine (1987)). The solid line is for run B1(a), the dotted line is for B1(b) and the dashed line is for B1(c). Notice that the dashed line for run B1(c) has $\beta(r) = 0$, as expected for initial conditions which are set to be isotropic. For the other runs, however, where the cusp contraction was performed numerically, some anisotropy has been introduced to the system. The amount of anisotropy introduced *increases* as the infall time is *reduced*; notice that the solid black line in figure 3 displays more anisotropy than the dotted line - particularly at small radii. Finally, notice that $\beta(r)$ actually becomes negative at \sim the halo scale length. This is because while the initially isotropic dark matter distribution will have $\beta(r) = 0$, some particles will be more radially anisotropic than others. After mass inflow, these particles will be more efficiently heated and pushed to larger radii. For mass inflow which produces a small anisotropy, as in this case, this can lead to a depletion in radially anisotropic particles at $\sim a_h$ and hence a negative value for $\beta(\sim a_h)$.

3.2.3 The effect of increasing the collapse factor - run B2

Run B2 (see figure 2) demonstrates the effect of increasing the collapse factor[§], defined as a_h/h_b (the ratio of the halo and baryon

[§] The nomenclature - collapse factor - comes from the assumption that the baryons initially have the same scale length as the dark matter (a_h) and

scale lengths). The initial conditions were as in run B1 but with $a_h = 50$ and hence with collapse factor $a_h/h_b = 50$. The data points and curves are as for run B1, with the contraction times, t_{cont} similarly marked. Table 1 shows that these runs required much higher numerical resolution, with 681,818 halo particles. This is because longer scale length halos put more of the mass (and hence the particles) out at large radii. Thus, to achieve the same local resolution as in run B1, we must increase the number of particles at the centre by increasing the total number of particles. As in run B1, the effect of changing the baryon infall time from the adiabatic case (plot B2(c)) to the non-adiabatic cases (plots B2(a) and B2(b)) produces shallower final density profiles. The effect, however, is magnified as compared with run B1. This is because the crossing time for the halo at h_b (now with a much longer scale length) has significantly increased (see equation 7) from ~ 4 units for run B1 to 16 units for run B2. Thus, in run B2(a), a contraction time of $t_{cont} = 15$ is much further away from adiabaticity than the same contraction time is in run B1(b): the effect is now large enough to produce significantly shallower density profiles after mass inflow too. As might be expected though, the longer inflow time run B2(b) is closer to adiabaticity than the short inflow time run B2(a) (compare the dot dashed and dotted lines for both of these runs).

The final density profiles after mass loss - even for an initial cusp contraction which is adiabatic - do not agree well with the heuristic, analytic, prediction presented in appendix A. This is, perhaps, not surprising since the analytic formula was derived by considering only the limiting cases of impulsive mass loss and adiabatic mass loss. For the impulsive case, the limiting behaviour was taken such that the system would become unbound if it suddenly lost half of its mass. For the extreme scenario presented in run B2, where there is relatively little central dark matter mass initially, this heuristic argument clearly breaks down.

For these extreme initial conditions, a core does form in all cases in the final halo density profile.

3.2.4 The effect of increasing the baryon fraction - run B3

Run B3 (see figure 2) demonstrates the effect of increasing the baryon fraction. The initial conditions were as in run B1 but with $M_h = 2$ and so $f_b = 0.33$. Now, as in run B2, a central core with scale length $\sim 1 - 2$ forms in the halo density profile. There is little difference in the contracted density profiles (dot-dashed lines) between the adiabatic (plot B3(b)) and non-adiabatic (plot B3(a)) infall cases, yet the crossing time at h_b for the halo is 8.4 units; dropping the mass in over 15 time units is clearly *not* a good approximation to the true adiabatic case. As with run B1, this is why, after mass loss, the density profile for the non-adiabatic inflow run B3(a) is shallower than that for the adiabatic case B3(b).

The adiabatic case, as in run B1, is reasonably well fit by the heuristic calculation for impulsive mass loss presented in appendix A. As with run B2, a core has formed in the final density profile after mass loss for the non-adiabatic infall (plot B3(a)). The similarity between runs B2 and B3 after mass loss should not be too surprising. The factor which really matters - the central mass of dark matter as compared with the initial central baryonic mass - is very low in both cases. For run B2 this is achieved by pushing most

of the dark matter out to large radii; for run B3 it is achieved by reducing the total halo mass.

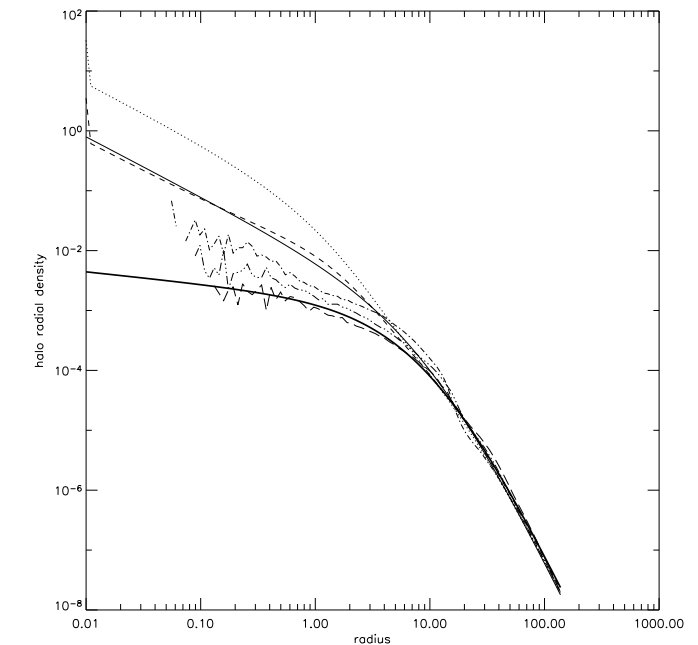


Figure 4. The effect of multiple inflows and outflows on the central halo density profile. The initial conditions for this run were as in table 1, while the units were as in section 2.2 and were for the cosmological mean values. In this run the baryons were dropped in slowly ($t_{cont} = 15$) and 95% removed quickly ($t_{ml} = 1$), *three times*. The resulting halo density profile after one two and three mass loss phases is marked by the dot-dashed, triple-dot dashed and long-dashed lines respectively. The thick solid line on this plot shows a density profile with central log-slope of $\alpha = 0.2$ for comparison with the simulation data. All of the other lines are as in figure 2.

of the dark matter out to large radii; for run B3 it is achieved by reducing the total halo mass.

3.2.5 The effect of multiple mass inflows and outflows - run B4

We have so far considered only the case of one slow mass infall phase followed by one impulsive mass loss phase. However, this process may have happened in dSph galaxies more than once, either at very early times or perhaps for some dSph throughout their history (the Carina, Leo I and Sagittarius dSphs all show evidence for continuous episodic star formation over the past ~ 14 Gyrs (Monelli et al. (2003), Hernandez et al. (2000) and Dolphin (2002)). As such, it is interesting to quantify the dynamical effect of such continuing mass inflow and outflow on a dSph galaxy on the underlying dark matter density profile.

Run B4 (see figure 4) demonstrates the effect of multiple mass loss phases punctuated by periods of slow accretion. The initial conditions were as in table 1 and represent the cosmological mean, with $f_b = 0.17$ (Spergel et al., 2003). In this run the baryons were dropped in slowly ($t_{cont} = 15$) and 95% removed quickly ($t_{ml} = 1$), *three times*. The resulting halo density profile after one two and three mass loss phases is marked by the dot-dashed, triple-dot dashed and long-dashed lines respectively. The thick solid line on this plot shows a density profile with central log-slope of $\alpha = 0.2$ for comparison with the simulation data. All of the other lines are as in figure 2.

Notice that after one mass inflow and outflow phase, as with run B1, the central dark matter density after mass loss is shallower than in the initial conditions (see the dot-dashed line compared with the solid line). It is this asymmetry which, when iterated three times, produces the much shallower central density profile in figure 4 (long-dashed line). The central density profile after three mass loss events is reasonably well fit by a shallower central dark matter slope with $\alpha \sim 0.2$ (see the thick solid line). Even after two such mass loss events, the central dark matter density profile has a central core (see triple-dot-dashed line). The ‘core size’ for the final density profile in figure 4, for both two and three mass loss events is $\sim 1 - 2$ baryon scale lengths. This translates to a ~ 1 kpc core for a dSph at the present epoch with scale length 1kpc.

3.3 The baryon surface density profile

In this section we consider the dynamical effect of mass loss from two-component galaxies, initially in equilibrium, on the surface density profile and projected velocity dispersion of the baryons. It is important to quantify the effect of mass loss on these observational signatures since these can then be compared with measurements from dwarf galaxies in the Local Group (see section 5).

The initial conditions used in this section were for a generalised Hernquist spheroid for the baryons (see equation 2) and a Hernquist profile for the dark matter (see equation 3). The generalised Hernquist profile was useful for the baryons as it allows for an easy parameterisation of a wide range of initial surface density profiles. The baryons were set up initially to be fully pressure supported with no internal angular momentum. This choice was motivated by the results from section 3.1 which suggest that spatially random mass loss produces a small perturbation on the total internal angular momentum in dSph galaxies, and by observations from the Local Group which suggest that dSph galaxies at the present epoch have very little internal angular momentum (see section 1). However, when rotating initial conditions were used, similar results to the non-rotating cases were obtained. As such, we present only the angular momentum free models here.

Similarly, while many other runs were also performed to demonstrate that the results are not sensitive to the choice of initial baryon or dark matter density profiles, for brevity we present only the key runs which illustrate the main points of interest.

The simulations are labelled, in order of discussion, from C1 to C5. Unless otherwise stated, all of the runs had the same initial conditions as run C1 but vary the outflow time and/or allow for baryon dissipation and collapse as in section 3.2 before mass loss. The initial conditions for all of the runs are summarised in table 1.

Overlaid on the simulation results are also analytic calculations for the response of the baryons to an impulsive gas mass loss detailed in appendix B. As with section 3.2, the analytic calculations provide a useful independent check of the numerical code while also highlighting the important physics.

3.3.1 Impulsive outflow - runs C1 and C2

Figure 5, top two rows, show the results for runs C1 and C2. The purpose of these simulations was to see whether, for fast mass loss from a galaxy in which the baryons initially dominate the central potential, the baryons retain information about their initial density profile and velocity dispersion.

In these runs, the halo was not adiabatically contracted to account for the presence of the baryons. This allowed the initial con-

ditions to be carefully controlled: we ensured that the velocity distribution before mass loss for both the baryons and the dark matter was isotropic.

After mass loss, the surface density profile of the baryons in both runs C1 and C2 (crosses, left panel) are now well fit by an exponential (solid straight line), irrespective of the initial conditions.

The dashed line in the left panel of figure 5 shows the post-mass loss baryon surface density profile calculated analytically for impulsive mass loss as in appendix B. As can be seen, this analytic calculation provides a good fit to the simulation data over many baryon scale lengths. This good agreement highlights two important points: firstly, that the numerical code is producing sensible results; and secondly, that the mechanism driving the change in surface density profile is the change in orbital structure of the baryons produced by the fast mass loss (see appendix B). For fast changes to the local potential, orbital structure is no longer conserved - all orbits become more energetic and, therefore, more radial (since angular momentum will still be conserved for symmetric changes). The time integration of these orbits leads to an approximately exponential surface density profile over many radii after mass loss (see appendix B).

The middle panels of figure 5 show the baryon velocity anisotropy, $\beta(r)$, after mass loss. The first thing to note is that the baryons, which were initially isotropic before mass loss with $\beta(r) = 0$, now show significant radial anisotropy as a result of the mass loss. The second thing to note is that in all cases there is a drop in $\beta(r)$ at \sim the halo scale length ($a_h=10$ units in figure 5). After mass loss, at $\sim a_h$, the baryons move from being radially anisotropic as a result of the mass loss to being closer to their initial conditions with $\beta(r) \sim 0$. This is because the halo scale length sets the scale at which the changes to the central potential caused by baryon mass loss become negligible.

For two of the simulations - runs C2 and C4 - $\beta(r)$ actually becomes *negative* at $\sim a_h$ after mass loss. This occurs for similar reasons to $\beta(r)$ becoming negative at large r for the dark matter halo in figure 3: the more radially anisotropic baryon particles before mass loss are preferentially moved towards larger radii after mass loss. For the simulations where the anisotropy introduced by the mass loss is small (as is the case for runs C2 and C4), this can deplete the fraction of radially anisotropic particles at \sim the halo scale length after mass loss, leading to a negative $\beta(r)$.

After the drop point at $\sim a_h$, $\beta(r)$ rises steeply towards unity - indicating highly radial orbits. This is because at these large radii, there are now *no particles left from the original baryon distribution before mass loss*. The particles which populate these radii after mass loss are those on highly radial orbits which have moved outward as a result of the mass loss.

The right panels of figure 5 show the projected baryon velocity dispersion, $\sqrt{v_p^2(R)}$, before mass loss (dotted lines) and after mass loss (data points). There are three important features to notice:

1. $\sqrt{v_p^2(R)}$ is significantly reduced at radii interior to $\sim a_h$. This is because particles which before mass loss had high kinetic energy, become easily unbound after mass loss and move outward to larger radii.
2. As with $\beta(r)$, at $\sim a_h$ where the halo begins to dominate the local potential, the projected velocity dispersions converge on the initial condition values.
3. At very large radii, in run C1 there is a sharp drop in the pro-

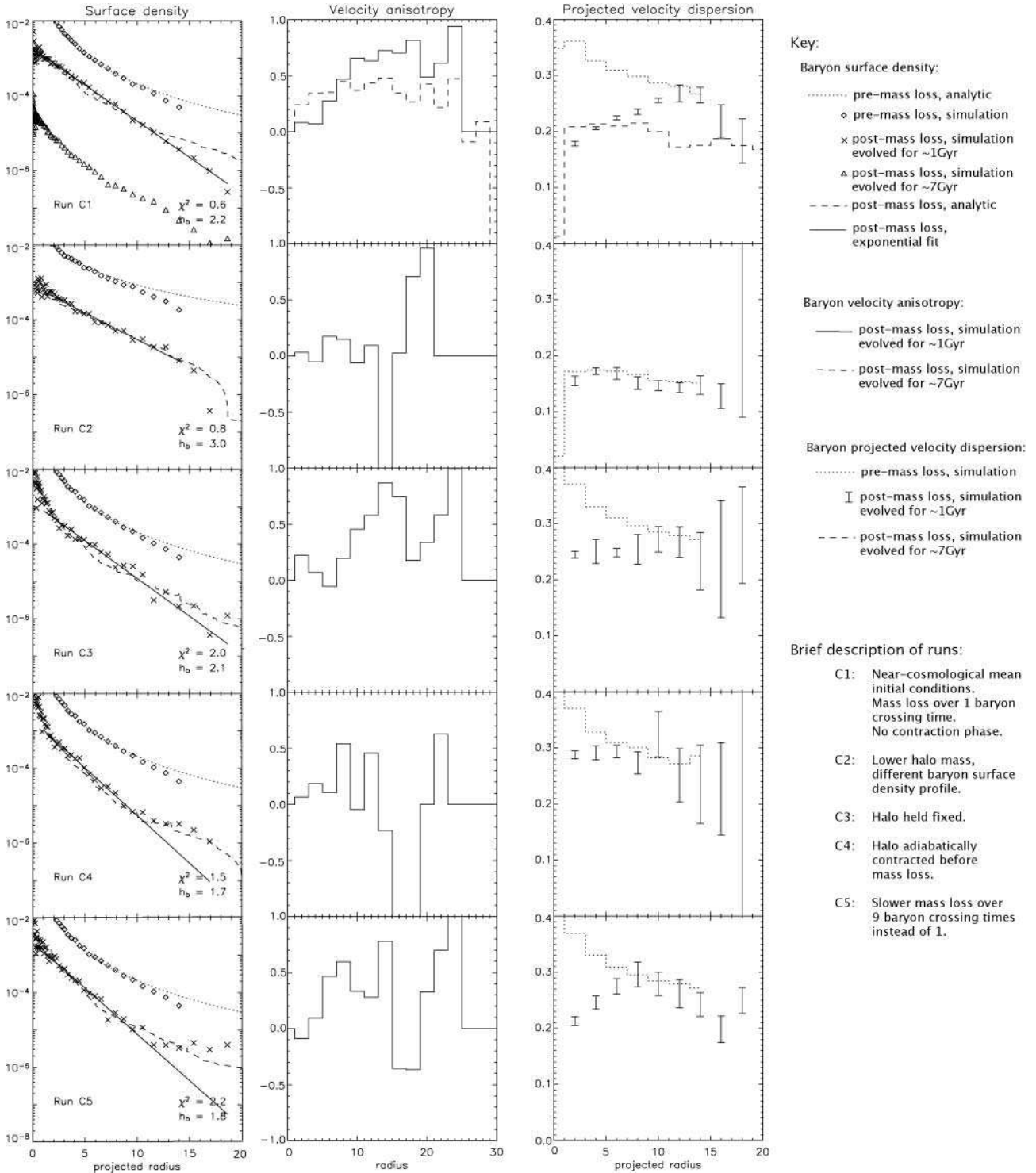


Figure 5. The response of the baryons to mass loss from the baryons, runs C1-C5. The left panel shows the baryon surface density profile integrated along the z -axis before (diamonds) and after (crosses) the mass loss. The dotted lines are the initial analytic surface density profiles, the dashed lines are the analytic predictions for the final density profile after mass loss in the impulsive limit. The straight solid line is an exponential fit to the final baryon surface density profile (crosses). χ^2 for the fit is shown in the bottom right of the surface density plot, along with the fitted baryon scale length: h_b . The middle panel shows the baryon velocity anisotropy, $\beta(r)$, as a function of radius after the mass loss. The right panel shows the projected velocity dispersion as a function of projected radius for the baryons before mass loss (dotted lines) and after mass loss (data points), averaged over 20 different projection angles. The error bars are determined from the standard deviation between results obtained from different projection axes. All of the runs were evolved for 15 time units (~ 1 Gyr) after mass loss except for run C1 which was also evolved for a further 100 time units (see the triangles in the left panel and the dashed lines in the middle and right panels) to test for equilibrium. The triangles have been offset from their true value by 10^{-2} for clarity. The initial conditions for the runs are as in table 1, while the units are as in section 2.2. The initial conditions for run C1 were a Hernquist, non rotating spheroid of stars with $M_b = h_b = 1$, embedded in a Hernquist halo with $M_h = a_h = 10$. The rest of the runs consider the effect of altering either these initial conditions or the mass loss rate as detailed in the text.

jected velocity dispersion *beyond the edge of the initial baryon distribution*. As discussed above, this is caused by these radii being populated solely by particles on highly radial orbits.

Finally, run C1 was also evolved for a further 100 time units (~ 7 Gyrs) after mass loss to test for equilibrium (see triangles and dashed lines in the first row of figure 5). While the halo was found to evolve very little over this time, the baryons are still evolving since particles which became unbound after mass loss take some time to leave the system. Recall from section 2.4, that we have not studied in general the longer term evolution of these dynamical models since it is likely that over these longer times external tidal effects become important and should be included in the analysis. However, notice that over longer times, the baryons continue to slowly expand, with the radial anisotropy spreading to smaller radii as highly radial particles return from larger radii. There are now two pronounced distributions: interior to the original particle distribution, the profile is still approximately exponential; exterior to the original distribution, the particles are more radial, causing a drop in the projected velocity dispersion and a break in the surface density profile at $\sim a_h$.

3.3.2 Impulsive outflow in a rigid halo potential - run C3

Figure 5, row 3, shows the results for run C3, which was the same as run C1 but with the halo held fixed, forming a rigid potential. The purpose of this run was to test whether the formation of exponential surface density profiles depends only on the mass loss rate and not the response of the dark matter halo. As can be seen from figure 5, with the halo held fixed, the final surface density profile of the baryons is still reasonably well fit ($\chi^2 = 2$) by an exponential. However, the fit is much poorer than in run C1. The baryons retain much more information about their initial condition density profile. This suggests that the reduced effect of the mass loss (caused by holding the halo fixed) leads to a smaller rearrangement of the baryon surface density profile.

The velocity structure for run C3 is qualitatively similar to that in run C1 (see figure 5): the mass loss causes radial anisotropy to be introduced to the remaining baryons; a sharp drop in $\beta(\sim a_h)$ and a subsequent rise leads to a drop in the projected velocity dispersion at $\sim a_h$.

3.3.3 Slow inflow, Impulsive outflow - run C4

Figure 5, row 4, shows the results for the run C4, in which the baryons were adiabatically contracted using the prescription set out in appendix A, after which 95% of them were removed quickly in 1 time unit. The initial conditions for this run are otherwise identical to those for run C1.

This run is interesting as it approximates the case where the baryons collapse dissipatively on some timescale before mass loss.

As with the fixed halo model, run C3, the post-mass loss baryon surface density distribution in runs C4 is reasonably well fit by an exponential profile over many radii with $\chi^2 = 1.5$. However, as with run C3, the baryons still retain more memory of their initial conditions than in run C1. Where the effect of the mass loss is reduced, in this case due to the halo contraction before mass loss, the final baryon surface density profile is closer to the initial conditions.

The velocity structure is qualitatively similar to run C2 (see figure 5). This again reflects the fact that the baryonic mass loss

has a smaller affect on the central potential in run C4 as compared with run C1.

3.3.4 Varying the outflow rate - runs C5

Figure 5, row 5, shows the results for the run C5, in which 95% of the baryons were removed over a longer outflow time of $t_{ml} = 9$. The purpose of this simulation was to quantify how fast the mass loss must be in order to produce a surface density profile which is well fit by an exponential. The initial conditions for this run were in all other respects identical to run C1.

As can be seen from figure 5, as the outflow rate is reduced the surface density profile of the baryons more closely resembles the initial conditions. For $t_{ml} = 9$, the baryon surface density profile is now well fit by an exponential only interior to $\sim a_h$, with a break in the exponential profile at this radius. Notice, however, that the analytic calculation from appendix B (dashed line) still provides a good fit.

The baryon velocity anisotropy and velocity dispersion for run C5 (see figure 5) follow the same trend as the baryon surface density: as the outflow time increases, the anisotropy introduced by the mass loss is reduced, the drop in $\beta(r)$ moves to smaller radii and the projected velocity dispersion becomes smoother (although the feature corresponding to the drop and subsequent rise in $\beta(r)$ remains).

3.4 Why do exponential surface density profiles form?

As demonstrated above, where mass loss significantly and rapidly alters the central potential, approximately exponential surface density profiles form after mass loss for a wide range of initial conditions. The move from isotropic to radial orbits for the baryons represents half of the answer to why this occurs. But questions remain: what determines the final energy distribution of the baryons after mass loss; and why, over many different initial conditions does this lead in all cases to approximately exponential surface density profiles?

Rapid changes in the potential of a galaxy will lead to violent relaxation in the remaining stars and dark matter, which causes the system to move towards a Maxwellian distribution (with temperature proportional to mass) irrespective of the initial conditions (Lynden-Bell, 1967). It may be simply shown that the surface density profile of a Maxwellian distribution embedded in a Hernquist potential is approximately exponential over a wide range of radii (see appendix C). Furthermore, while Maxwellian distributions are isotropic and the baryons after mass loss here are clearly not, it may be demonstrated that the inclusion of anisotropy destroys the exponential-like surface density profiles only if the final distribution of baryons becomes strongly anisotropic at all radii. This is not the case in these simulations (see also appendix C).

We conclude that the ultimate cause of the exponential-like surface density profiles in these models is the violent relaxation of the surviving baryons after mass loss and the move towards a Maxwellian distribution. At large radii beyond $\sim a_h$, where the baryons are highly anisotropic after mass loss and do not reach a Maxwellian distribution, a second population forms, causing a break in the surface density profile and a drop in the projected velocity dispersion near the halo scale length.

4 DISCUSSION

In this section we discuss the simulation results in relation to other works on mass loss already in the literature and demonstrate that this study complements and expands on the existing material. We also highlight and clarify the assumptions inherent in this work.

4.1 Comparison with previous work

Gnedin & Zhao (2002), Navarro et al. (1996a) and Gelato & Sommer-Larsen (1999) have all looked at the effect on a Hernquist halo density profile of removing a baryonic disc. The crucial differences with our study here are as follows:

1. The main contribution of this work is to analyse the baryons left behind after mass loss, quantifying their angular momentum, surface density profile and velocity structure. This then allows us to compare the galaxy dynamical evolution models presented here with observations (see section 5). This has not been covered by previous authors.

2. We start with both spherically symmetric pressure supported and axisymmetric rotationally supported baryonic profiles as options for the progenitors of dwarf spheroidal galaxies. The earlier studies start with a disc with some net angular momentum. As such, the collapse factor in the models presented here is a free parameter, whereas in the previous literature, it is constrained by the initial angular momentum profile of the baryons (although Gnedin & Zhao (2002) do discuss angular momentum-free collapse).

3. We simulate the contraction of the central dark matter cusp and compare this with the adiabatic, analytic prediction. Gnedin & Zhao (2002) impose the analytic result on their initial conditions for the simulations, while Gelato & Sommer-Larsen (1999) and Navarro et al. (1996a) use only a numerical cusp contraction method. As demonstrated in section 3.2, while non-adiabatic inflow can often produce density profiles which are well fit by the adiabatic form, the non-isotropic velocity distribution created by the inflow leads to shallower density profiles after mass loss. Thus it is important to consider the case of faster mass inflow as compared with the true adiabatic case.

4. We use this numerical cusp contraction method to study the effect of *multiple* mass loss phases punctuated by periods of slow accretion. This can produce cores from cuspy dark matter distributions, even with cosmological initial conditions.

5. We perform fully 3D N-body simulations with non-rigid disc and halo potentials. Gelato & Sommer-Larsen (1999) do the same, but at a lower resolution (40,000 particles). Navarro et al. (1996a) use a live halo but a rigid disc potential, and again at lower resolution (10,000 particles). Finally Gnedin & Zhao (2002) use a 1D shell code for their simulations. This has the advantage that it does not require any force softening, but the disadvantage that it is only 1D (and so, for example, the velocity distribution is necessarily isotropic at all times).

Gnedin & Zhao (2002) found that mass loss from the baryons produced a much smaller effect on the central density profile of the dark matter than was found by Navarro et al. (1996a) and Gelato & Sommer-Larsen (1999). They suggest that this could be due to resolution, but the differing nature of the codes employed made

these comparisons difficult. In order to shed some light on this issue, we re-simulated at *lower* resolution, with 10,000 particles, the run B1(c), where the baryons were contracted analytically and then 95% were removed very quickly. We found that, despite the larger Poisson errors, the results were consistent with the higher resolution run: no core was found to form in the dark matter central density after mass loss. It seems that another difference between the studies of Gnedin & Zhao (2002) and Navarro et al. (1996a) must be acting: we suggest that this is the baryon dissipational inflow rate. Both Navarro et al. (1996a) and Gelato & Sommer-Larsen (1999) numerically contract their dark matter cusps. As demonstrated in section 3.2, this leads to shallower cusps after mass outflow. The differences between these previous studies in the literature is then likely to be a combination of numerical resolution effects and the different methodologies which they assumed for the mass inflow phase for the baryons.

This view is further supported by Jesseit et al. (2002) who looked at the effects of non-adiabatic inflow on the contraction of a dark matter cusp. They find, similarly to the results presented here, that fast inflow can lead to shallower contraction than the adiabatic prediction, although they do not analyse the orbital structure of the dark matter before and after mass inflow. This last point is critical since density profiles which *appear* to be adiabatic after mass inflow can have anisotropic velocity distributions which lead to an increased response after mass loss.

4.2 Model assumptions

Before discussing the results and their relation or otherwise to real dSph galaxies, it is important to recall and to justify the assumptions we have made both explicitly and implicitly in this study. We list the main assumptions below and discuss them in turn:

1. We assumed that dSph galaxies comprise a baryonic component and a dark matter component and that the galaxy, before mass loss, is in virial equilibrium.

2. We assumed that the dark matter component of the galaxy is spherical and symmetric and can be parametrised by a Hernquist profile or a truncated isothermal sphere. Furthermore we assumed that the initial velocity structure of the halo before baryonic mass infall is isotropic.

3. We assumed that the baryonic component of the galaxy can be parametrised by a spherical, generalised Hernquist profile, or by a rotationally supported exponential disc.

The important assumption here is in the initial conditions used: an isotropic galaxy in equilibrium. This is perhaps unlikely to be the case for a real proto-galaxy. However, in terms of the magnitude of any feedback due to mass loss from the baryons, starting with equilibrium initial conditions represents the extremum case. This is because this allows the baryons to collapse and dominate the central potential *before* any mass loss occurs. Mass loss which occurs at the same time as baryonic collapse would produce weaker effects than those discussed here, all other things being equal, since the baryons would be less centrally concentrated at the point of mass loss.

The assumption of initial isotropy is also critical. As discussed above, strongly radially anisotropic velocity distributions become more easily unbound as a result of rapid changes in the local potential (such as is caused by fast mass loss). Thus initial radial

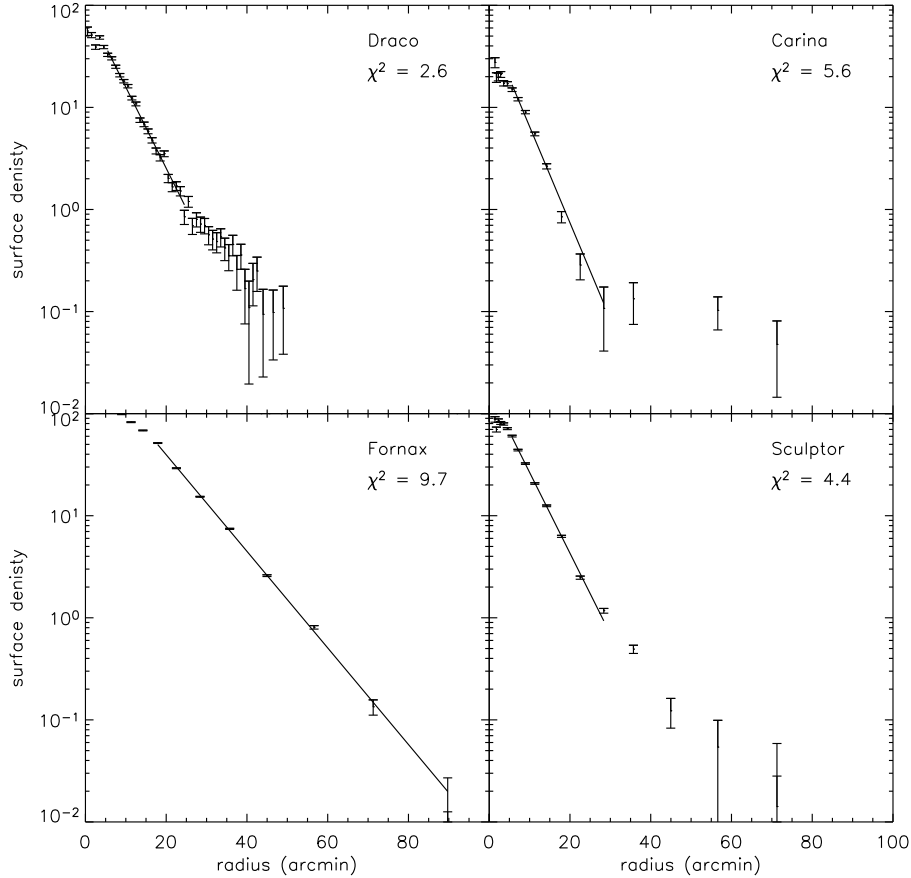


Figure 6. The surface density profiles of four Local Group dSph galaxies. The solid lines are exponential fits to the surface density profiles over a range of radii. χ^2 for each of the fits is marked in the top right hand corner of each plot. The data were taken from Irwin, private correspondence (Draco) and Walcher et al. (2003) (Carina, Fornax and Sculptor).

anisotropy would *increase* the dynamical effects of mass loss on the remaining stars and dark matter.

5 COMPARISON WITH OBSERVATIONS

5.1 Angular momentum

In section 3.1, we considered the effect of mass loss on the angular momentum distribution in dwarf galaxies. The best studied Local Group dSph galaxy, Draco, is not rotating at all at the 3-sigma level (Kleyna et al., 2001); the other Local Group dSph galaxies also show near complete pressure support, with very little rotation (see e.g. Mateo (1998)). However, if the progenitor galaxies to dSph at the present epoch are consistent with scale-free Λ CDM cosmology, then they should form from gas with significant global internal angular momentum (see e.g. Bullock et al. (2001) and Colin et al. (2003)). Could random or biased mass loss explain this angular momentum discrepancy?

Only three simulations produced significant angular momentum loss. The first, run A6, had almost no dark matter initially interior to the baryons, while the initial baryon distribution was mostly in pressure support, with $v_r/\sigma = 0.8$. This run, which represented the most extreme case for random mass removal, was then already a low-angular momentum system before mass loss.

The other simulations which produced significant angular momentum loss were the biased mass loss runs: runs A7 and A8. These preferentially removed mass at large radii, thus removing much more of the initial angular momentum for a given mass loss fraction. While this type of mass loss would not be caused by supernovae explosions which would be expected to remove preferentially the *low* angular momentum gas (see e.g. Maller & Dekel (2002)); this type of mass loss could correspond to strong tidal stripping caused as a proto-dSph galaxy passes close to a larger nearby galaxy (see e.g. Mayer et al. (2001)). However, both runs A7 and A8 left remnants which had a larger final angular momentum than that measured in the Draco dSph galaxy (Kleyna et al., 2001).

It is clear that in order to model the angular momentum distribution of the Local Group dwarf galaxies, these galaxies must be simulated in a cosmological context where the timescales for gas dissipation, dark matter collapse, merging and feedback are all comparable. However, the results from this study suggest that the origins of low angular momentum *tidally isolated* systems are not a result of gas mass loss. Furthermore, even biased mass loss scenarios such as tidal stripping would leave a measurable amount of angular momentum behind if dSph galaxies really formed from high-angular momentum gas discs.

5.2 The effect of mass loss on the central dark matter distribution

In section, 3.2, we considered the effect of mass loss from the baryons on the underlying dark matter distribution. In particular we considered whether or not a dark matter cusp with log slope, $\alpha = -1$, such as is predicted by cosmological simulations of dark matter halo formation, could survive one or many phases of mass loss from the baryons. On the smallest scales, from the Milky Way to dIrr and LSB galaxies, the central dark matter density profile is well fit inside ~ 1 kpc by an approximately constant density *core* (see e.g. de Blok et al. (2001), Salucci & Borriello (2002) and Binney & Evans (2001)), rather than the $1 < \alpha < 1.5$ log-slope predicted by current cosmological simulations (see e.g. Klypin et al. (2001), Ghigna et al. (2000) and Navarro et al. (1996b)). Furthermore, there is recent evidence that this problem persists on the smallest scales, within dSph galaxies (Kleyna et al., 2003). It is interesting, then, to consider whether or not extreme mass loss from the baryons can resolve the cusp-core problem by lowering the central dark matter density.

In all of the simulations in section 3.2 the dark matter responded dynamically to the time dependent potential, provided that baryons dominated the central potential initially, and provided that the mass loss was rapid (of the order a baryon crossing time). However, if the dark matter was allowed to contract adiabatically in response to the slow dissipation and collapse of the baryons, the final effect after mass loss on the density profile of the halo was small. Reducing the inflow time of the baryons and moving away from the adiabatic regime produced shallower final density profiles after mass loss but, for cosmologically consistent initial conditions, the final halo density profiles retained central slopes which were close to the initial conditions - although with lower central normalisations (see for example runs B1 and B4). Only for the two extreme initial condition simulations (B2 and B3), did the final halo density profile exhibit a shallower central density *slope*. The similarity in this respect between these two simulations is not surprising: they both had a very low central mass of dark matter before mass loss as compared with the mass of the baryons. For run B2, this was achieved by increasing the halo scale length and moving all of the mass out to larger radii. For run B3, this was achieved by reducing the total halo mass to be just two times the total mass of the baryons initially.

While these extreme simulations can transform central dark matter density cusps into cores, neither of them provides a neat solution to the cusp-core problem. This is because for run B2, the scale length of the halo is so large initially, ($a_h/h_b = 50$), that it must either correspond to a galaxy much smaller than present-day dSph galaxies, or correspond to the formation of very extended low-concentration halos, which are not predicted to form in cosmological simulations. Put more quantitatively, cold dark matter simulations predict that halos forming on the smallest scales should have concentration parameters greater than ~ 10 (Navarro et al., 1996b), which fixes the collapse factor to be *at most* $a_h/h_b \sim 10$ for a halo of mass $10^{10} M_\odot$. Thus, although there is no current *observational* constraint on the collapse parameter, there is a self-consistency constraint from numerical simulations. Similarly, run B3 requires an initial baryon fraction of $f_b = 0.33$ which is much larger than the cosmological mean value of $f_b = 0.17$ (Spergel et al., 2003). This implies a situation where a halo accumulates an initial over-abundance of baryons, then loses a very significant amount of its baryonic mass. The baryonic mass of a progenitor to

such a dSph galaxy would be some $\sim 10^8 M_\odot$, assuming a current baryonic mass of $\sim 10^6 M_\odot$ (Kleyna et al., 2001).

While single mass loss events do not significantly perturb the underlying dark matter distribution, *multiple* mass loss events can cause significant flattening of the central dark matter density for initial conditions which represent the cosmological mean (see run B4). This is due to the iterative asymmetry introduced by a slow, *but non-adiabatic* inflow followed by a fast, impulsive, mass loss. Thus, if dSph galaxies have undergone two or more violent star formation bursts, with rapid baryon re-accretion then their central dark matter density profile could have been transformed from a r^{-1} cusp into a $\sim r^{-0.2}$ core.

5.3 The baryon surface density profile

Figure 6 shows a plot of the surface density profiles of four Local Group dSph galaxies (data were taken from Wilkinson et al. (2004) and Walcher et al. (2003)). Notice that all of the profiles, over a wide range of radii, are reasonably well fit by an exponential - especially the Draco dSph galaxy (χ^2 for the fits is shown in the top right hand corner of each plot). Notice further that three of the four profiles show a clear break in the surface brightness profile of the light at what may be a tidal radius (see e.g. Walcher et al. (2003), Mateo (1998) and Grebel et al. (2003)). The one galaxy which does not show such a break, Fornax, is also the galaxy furthest from the Milky Way at present (Mateo, 1998).

These profiles are qualitatively well fit by the simulation profiles in which exponential-like profiles form over a wide range of radii in all cases. In fact the ‘tidal feature’ could also be the result of mass loss. A break in the surface density profile was observed in all of the simulations either as a result of the long-time evolution of the baryons (see run C1), or as a result of slower (run C5) or less strong (runs C3 and C4) mass loss.

This is particularly interesting since several authors have proposed that the Local Group dSph galaxies may reside in much larger dark matter halos (see e.g. Hayashi et al. (2003)). If this were the case then their tidal radii would lie far beyond the luminous matter and the observed ‘tidal features’ in the surface density profiles would require another explanation. We propose here that one explanation for these features could be mass loss.

Finally, these results may scale up to larger elliptical galaxies. Trujillo et al. (2004) have recently shown that there is a strong correlation between the surface brightness profiles of elliptical galaxies and their absolute magnitudes: lower magnitude elliptical galaxies have more exponential-like surface density profiles. If the absolute magnitude of ellipticals is a good tracer of their total mass then this correlation could be explained by gas mass loss driven by feedback - either from star formation or from a central active nucleus. Feedback would then be more effective in less massive systems and so less massive, lower luminosity elliptical galaxies would have more exponential-like surface density profiles, as observed.

5.4 The baryon projected velocity dispersion

While the detailed form of the projected velocity dispersion after mass loss varied for different initial conditions, there was one common feature: the formation of a new, radially-biased, population of baryons beyond the original distribution after mass loss led, in all cases, to a drop in the projected velocity dispersion at $\sim a_h$, the halo scale length.

This is interesting since recent results from Wilkinson et al.

(2004) find just such a drop in the projected velocity dispersion for the Draco and UMi dSph galaxies.

The good qualitative agreement between both the surface density profiles and projected velocity dispersions (where measured) of the Local Group dSph galaxies and the dynamical models presented in this paper indicates that mass loss may be the primary evolutionary factor in determining the structure of dSph galaxies at the present epoch. To test this idea further, a next step towards building a more realistic model for the formation of the Local Group dSph galaxies should include the effect of an external tidal field from the proto-Milky Way; this will provide the subject of future work.

6 CONCLUSIONS

We have looked at the dynamical effect of baryonic mass loss from two-component galaxies comprising a dark matter halo and some baryons, initially in equilibrium. These initial conditions represent an extreme case; by studying this we have been able to quantify the potential importance of mass loss on astrophysically interesting observational signatures, such as the central dark matter density, internal angular momentum distribution and baryon surface density profile of these galaxies.

Our focus was on simulating the effects of mass loss on progenitors to what are currently dwarf spheroidal (dSph) galaxies. This is because these galaxies appear observationally to have lost a large fraction of their gas mass at some point in the past.

Our main findings are summarised below:

1. One impulsive mass loss event involving a sufficiently large fraction of the baryons will naturally produce a surface density profile in the remaining stellar component of a dSph which is well fit by an exponential over many scale lengths, in good qualitative agreement with observations of the Local Group dSphs. Furthermore, in nearly all models, a break is naturally found to form in the surface density profile at large radii, which could be easily mistaken for a feature of tidal origin. This lends support to the idea that the true tidal radius of the Local Group dSph galaxies may lie well beyond the observed light.
2. Mass loss naturally leads to a drop in the projected velocity dispersion of the light at around the halo scale length, also in good qualitative agreement with recent observations of the Draco and UMi dSph galaxies.
3. Two impulsive mass loss phases, punctuated by significant gas re-accretion, are found to be sufficient to transform a central density cusp in the dark matter profile into a near-constant density core. This may then provide the missing link between current cosmological simulations, which predict a central cusp in the dark matter density profile, and current observations, which find much shallower central density profiles.
4. Mass loss cannot account for the currently observed low angular momentum of the Local Group dSph galaxies. Thus, if local group dSph galaxies have spent most of their lifetime in tidal isolation from massive galaxies, then they cannot have formed from high angular momentum gas discs.

7 ACKNOWLEDGEMENTS

We would like to thank Lars Hernquist for his galaxy initialisation code and Jakob Walcher for the data for the Carina, Fornax and Sculptor galaxies. Finally we would like to thank Mark Wilkinson and the referee for useful comments which led to the completion of this manuscript. Part of this work was conducted on the SGI Origin platform using COSMOS Consortium facilities, funded by HEFCE, PPARC and SGI.

REFERENCES

- Barkana R. & Loeb A. 1999. *The Photoevaporation of Dwarf Galaxies during Reionization*, ApJ, 523, 54
- Barnes J. & Hut P. 1986. *A Hierarchical O(NlogN) Force-Calculation Algorithm*, Nature, 324, 446
- Benson A. J., Bower R. G., Frenk C. S., Lacey C. G., Baugh C. M., & Cole S. 2003. *What Shapes the Luminosity Function of Galaxies?*, ApJ, 599, 38
- Binney J. 2004. *On the origin of the galaxy luminosity function*, MNRAS, 347, 1093
- Binney J. & Tremaine S. 1987. *Galactic dynamics* (Princeton, NJ, Princeton University Press, 1987, 747 p.)
- Binney J. J. & Evans N. W. 2001. *Cuspy dark matter haloes and the Galaxy*, MNRAS, 327, L27
- Boily C. M. & Kroupa P. 2003a. *The impact of mass loss on star cluster formation - I. Analytical results*, MNRAS, 338, 665
- . 2003b. *The impact of mass loss on star cluster formation - II. Numerical N-body integration and further applications*, MNRAS, 338, 673
- Borriello A. & Salucci P. 2001. *The dark matter distribution in disc galaxies*, MNRAS, 323, 285
- Bullock J. S., Dekel A., Kolatt T. S., Kravtsov A. V., Klypin A. A., Porciani C., & Primack J. R. 2001. *A Universal Angular Momentum Profile for Galactic Halos*, ApJ, 555, 240
- Carigi L., Hernandez X., & Gilmore G. 2002. *Chemical evolution models of local dwarf spheroidal galaxies*, MNRAS, 334, 117
- Colin P., Klypin A., Valenzuela O., & Gottlober S. 2003. *Dwarf Dark Matter Halos* (astro-ph/0308348)
- de Blok W. J. G., McGaugh S. S., Bosma A., & Rubin V. C. 2001. *Mass Density Profiles of Low Surface Brightness Galaxies*, ApJ, 552, L23
- Dehnen W. 2000. *A Very Fast and Momentum-conserving Tree Code*, ApJ, 536, L39
- Dekel A., Arad I., Devor J., & Birnboim Y. 2003. *Dark Halo Cusp: Asymptotic Convergence*, ApJ, 588, 680
- Dekel A. & Silk J. 1986. *The origin of dwarf galaxies, cold dark matter, and biased galaxy formation*, ApJ, 303, 39
- Dekel A. & Woo J. 2003. *Feedback and the scaling relations of dwarf/LSB galaxies* (astro-ph/0210454)
- Dinescu D. I., Keeney B. A., Majewski S. R., & Girard T. M. 2004. *Absolute Proper Motion of the Fornax Dwarf Spheroidal Galaxy from Photographic and HST WFPC2 Data*
- Dolphin A. E. 2002. *Numerical methods of star formation history measurement and applications to seven dwarf spheroidals*, MNRAS, 332, 91
- Efstathiou G. 2000. *A model of supernova feedback in galaxy formation*, MNRAS, 317, 697
- Einasto J., Saar E., Kaasik A., & Chernin A. D. 1974. *Missing mass around galaxies - Morphological evidence*, Nature, 252, 111
- Ferguson H. C. & Binggeli B. 1994. *Dwarf elliptical galaxies*, A&A Rev., 6, 67
- Gelato S. & Sommer-Larsen J. 1999. *On DDO 154 and cold dark matter halo profiles*, MNRAS, 303, 321
- Ghigna S., Moore B., Governato F., Lake G., Quinn T., & Stadel J. 2000. *Density Profiles and Substructure of Dark Matter Halos: Converging Results at Ultra-High Numerical Resolution*, ApJ, 544, 616
- Gnedin O. Y. & Zhao H. 2002. *Maximum feedback and dark matter profiles of dwarf galaxies*, MNRAS, 333, 299
- Governato F., Mayer L., Wadsley J., Gardner J. P., Willman B., Hayashi E., Quinn T., Stadel J., & Lake G. 2004. *The Formation of a Realistic Disk Galaxy in Λ -dominated Cosmologies*, ApJ, 607, 688
- Grebel E. K. 1999, in IAU Symposium, 17–+
- Grebel E. K., Gallagher J. S., & Harbeck D. 2003. *The Progenitors of Dwarf Spheroidal Galaxies*, AJ, 125, 1926
- Hayashi E., Navarro J. F., Taylor J. E., Stadel J., & Quinn T. 2003. *The Structural Evolution of Substructure*, ApJ, 584, 541
- Hernandez X., Gilmore G., & Valls-Gabaud D. 2000. *Non-parametric star formation histories for four dwarf spheroidal galaxies of the Local Group*, MNRAS, 317, 831
- Hernquist L. 1990. *An analytical model for spherical galaxies and bulges*, ApJ, 356, 359
- . 1993. *N-body realizations of compound galaxies*, ApJS, 86, 389
- Ikuta C. & Arimoto N. 2002. *Extended star formation in dwarf spheroidal galaxies: The cases of Draco, Sextans, and Ursa Minor*, A&A, 391, 55
- Jesseit R., Naab T., & Burkert A. 2002. *The Validity of the Adiabatic Contraction Approximation for Dark Matter Halos*, ApJ, 571, L89
- Kazantzidis S., Magorrian J., & Moore B. 2004. *Generating Equilibrium Dark Matter Halos: Inadequacies of the Local Maxwellian Approximation*, ApJ, 601, 37
- Kleyna J. T., Wilkinson M. I., Evans N. W., & Gilmore G. 2001. *First Clear Signature of an Extended Dark Matter Halo in the Draco Dwarf Spheroidal*, ApJ, 563, L115
- Kleyna J. T., Wilkinson M. I., Gilmore G., & Evans N. W. 2003. *A Dynamical Fossil in the Ursa Minor Dwarf Spheroidal Galaxy*, ApJ, 588, L21
- Klypin A., Kravtsov A. V., Bullock J. S., & Primack J. R. 2001. *Resolving the Structure of Cold Dark Matter Halos*, ApJ, 554, 903
- Larson R. B. 1974. *Effects of supernovae on the early evolution of galaxies*, MNRAS, 169, 229
- Lynden-Bell D. 1967. *Statistical mechanics of violent relaxation in stellar systems*, MNRAS, 136, 101
- Mac Low M. & Ferrara A. 1999. *Starburst-driven Mass Loss from Dwarf Galaxies: Efficiency and Metal Ejection*, ApJ, 513, 142
- Maller A. H. & Dekel A. 2002. *Towards a resolution of the galactic spin crisis: mergers, feedback and spin segregation*, MNRAS, 335, 487
- Mateo M. L. 1998. *Dwarf Galaxies of the Local Group*, ARA&A, 36, 435
- Mayer L., Governato F., Colpi M., Moore B., Quinn T., Wadsley J., Stadel J., & Lake G. 2001. *Tidal Stirring and the Origin of Dwarf Spheroidals in the Local Group*, ApJ, 547, L123
- Merritt D. 1985. *Distribution functions for spherical galaxies*, MNRAS, 214, 25P
- Mihos J. C. & Hernquist L. 1994. *Triggering of starbursts in galaxies by minor mergers*, ApJ, 425, L13
- Monelli M., Pulone L., Corsi C. E., Castellani M., Bono G., Walker A. R., Brocato E., Buonanno R., Caputo F., Castellani V., Dall'Orta M., Marconi M., Nonino M., Ripepi V., & Smith H. A. 2003. *The Carina Project. II. Stellar Populations*, AJ, 126, 218
- Moore B., Katz N., Lake G., Dressler A., & Oemler A. 1996. *Galaxy harassment and the evolution of clusters of galaxies*, Nature, 379, 613
- Moore B., Lake G., & Katz N. 1998. *Morphological Transformation from Galaxy Harassment*, ApJ, 495, 139
- Naab T. & Burkert A. 2001, in ASP Conf. Ser. 249: The Central Kiloparsec of Starbursts and AGN: The La Palma Connection, 735–+
- Navarro J. F., Eke V. R., & Frenk C. S. 1996a. *The cores of dwarf galaxy haloes*, MNRAS, 283, L72
- Navarro J. F., Frenk C. S., & White S. D. M. 1996b. *The Structure of Cold Dark Matter Halos*, ApJ, 462, 563
- Odenkirchen M., Grebel E. K., Harbeck D., Dehnen W., Rix H., Newberg H. J., Yanny B., Holtzman J., Brinkmann J., Chen B., Csabai I., Hayes J. J. E., Hennessy G., Hindsley R. B., Ivezić Ž., Kinney E. K., Kleinman S. J., Long D., Lupton R. H., Neilsen E. H., Nitta A., Snedden S. A., & York D. G. 2001. *New Insights on the Draco Dwarf Spheroidal Galaxy from the Sloan Digital Sky Survey: A Larger Radius and No Tidal Tails*, AJ, 122, 2538
- Osipkov L. P. 1979. *Spherical systems of gravitating bodies with an ellipsoidal velocity distribution*, Pis ma Astronomicheskii Zhurnal, 5, 77
- Piatek S., Pryor C., Olszewski E. W., Harris H. C., Mateo M., Minniti D., Monet D. G., Morrison H., & Tinney C. G. 2002. *Proper Motions of Dwarf Spheroidal Galaxies from Hubble Space Telescope Imaging. I. Method and a Preliminary Measurement for Fornax*, AJ, 124, 3198
- Power C., Navarro J. F., Jenkins A., Frenk C. S., White S. D. M., Springel V., Stadel J., & Quinn T. 2003. *The inner structure of Λ CDM haloes - I. A numerical convergence study*, MNRAS, 338, 14
- Quinn T., Katz N., & Efstathiou G. 1996. *Photoionization and the formation of dwarf galaxies*, MNRAS, 278, L49
- Saha P. 1992. *Constructing stable spherical galaxy models*, MNRAS, 254, 132

- Salucci P. & Borriello A. 2002. *The Intriguing Distribution of Dark Matter in Galaxies* (astro-ph/0203457)
- Schwarzschild M. 1979. *A numerical model for a triaxial stellar system in dynamical equilibrium*, ApJ, 232, 236
- Schweitzer A. E. & Cudworth K. M. 1996. *The Absolute Proper Motion of the Ursa Minor Dwarf Spheroidal Galaxy*, Bulletin of the American Astronomical Society, 28, 835
- Schweitzer A. E., Cudworth K. M., Majewski S. R., & Suntzeff N. B. 1995. *The Absolute Proper Motion and a Membership Survey of the Sculptor Dwarf Spheroidal Galaxy*, AJ, 110, 2747
- Silk J. & Rees M. J. 1998. *Quasars and galaxy formation*, A&A, 331, L1
- Spergel D. N., Verde L., Peiris H. V., Komatsu E., Nolte M. R., Bennett C. L., Halpern M., Hinshaw G., Jarosik N., Kogut A., Limon M., Meyer S. S., Page L., Tucker G. S., Weiland J. L., Wollack E., & Wright E. L. 2003. *First-Year Wilkinson Microwave Anisotropy Probe (WMAP) Observations: Determination of Cosmological Parameters*, ApJS, 148, 175
- Springel V., Yoshida N., & White S. D. M. 2001. *GADGET: a code for collisionless and gasdynamical cosmological simulations*, New Astronomy, Volume 6, Issue 2, p. 79-117., 6, 79
- Steinmetz M. 1999. *Numerical Simulations of Galaxy Formation*, Ap&SS, 269, 513
- Subramanian K., Cen R., & Ostriker J. P. 2000. *The Structure of Dark Matter Halos in Hierarchical Clustering Theories*, ApJ, 538, 528
- Tolstoy E., Venn K. A., Shetrone M., Primas F., Hill V., Kaufer A., & Szeifert T. 2003. *VLT/UVES Abundances in Four Nearby Dwarf Spheroidal Galaxies. II. Implications for Understanding Galaxy Evolution*, AJ, 125, 707
- Trujillo I., Burkert A., & Bell E. F. 2004. *The Tilt of the Fundamental Plane: Three-Quarters Structural Nonhomology, One-Quarter Stellar Population*, ApJ, 600, L39
- van den Bergh S. 1999. *The local group of galaxies*, A&A Rev., 9, 273
- van den Bosch F. C., Burkert A., & Swaters R. A. 2001. *The angular momentum content of dwarf galaxies: new challenges for the theory of galaxy formation*, MNRAS, 326, 1205
- Walcher C. J., Fried J. W., Burkert A., & Klessen R. S. 2003. *About the morphology of dwarf spheroidal galaxies and their dark matter content*, A&A, 406, 847
- White S. D. M. & Rees M. J. 1978. *Core condensation in heavy halos - A two-stage theory for galaxy formation and clustering*, MNRAS, 183, 341
- Wilkinson M. I. et al. 2004. *Kinematically Cold Populations at Large Radii in the Draco and Ursa Minor Dwarf Spheroidals*
- Zhao H. 1996. *Analytical models for galactic nuclei*, MNRAS, 278, 488

APPENDIX A: THE RESPONSE OF A DARK MATTER HALO TO GAS COLLAPSE AND GAS MASS LOSS

In this appendix we briefly outline an analytic calculation to determine the response of a Hernquist dark matter halo (see equation 3) to the adiabatic dissipation and collapse and subsequent mass loss of some baryons. The calculation is similar to that set out in Gnedin & Zhao (2002), but using a pressure supported Hernquist profile for the initial conditions for the baryons. As such, we highlight only the differences here.

A1 The baryon dissipation and collapse phase

To model the adiabatic contraction of the central dark matter, we assume that the baryons and the dark matter start out with the same distribution - a Hernquist profile (see equation 3) and that the dark matter particles lie on a collection of randomly oriented circular orbits. The baryons then collapse to form a smaller Hernquist profile, with scale length h_b and mass M_b .

If the collapse conserves both the angular momentum of a dark

matter particle's orbit and the dark matter mass interior to its orbit then it can be shown that:

$$\frac{C}{b}a^3 + \left(\frac{2C}{b} - 1\right)a^2 + \left(\frac{C}{b} - 2\right)a - (1 + K(1 + b)^2) = 0 \quad (\text{A1})$$

where

$$C = \frac{a_h}{(1 - f_b)h_b} \quad (\text{A2})$$

$$K = \frac{f_b}{1 - f_b} \quad (\text{A3})$$

and r_i and r_j are the pre and post-collapse radii; a_h is the initial baryon scale length before collapse, which is also the halo scale length; M_h is the halo mass; $f_b = \frac{M_b}{M_b + M_h}$ is the baryon fraction; $a = h_b/r_j$ and $b = a_h/r_i$.

The final mass distribution, $M_{dm,j}(r_j)$, and density distribution can then be found by solving equation A1 numerically and using mass conservation.

A1.1 Adiabatic and instantaneous winds

We follow the prescription in Gnedin & Zhao (2002) and use an heuristic formula for the impulsive mass loss case. The formula results from considering the limiting cases of adiabatic mass loss and the limiting case of impulsive mass loss, where it is assumed that the system becomes unbound if it instantly loses half of its baryonic mass (Gnedin & Zhao, 2002). As shown in section 3.2, this formula provides a good fit to the simulation data in the appropriate limits. Following Gnedin & Zhao (2002), then, we have:

$$r_f = \frac{r_j}{(1 - f_W(r_j))^{1 + \frac{k}{4}} (1 - 2^k \delta f_b)^{\frac{k}{4}}} \quad (\text{A4})$$

where

$$f_W(r_j) = \frac{\delta M_b(r_j)}{M_{dm}(r_j) + M_b(r_j)} \quad (\text{A5})$$

and $0 \leq k \leq 1$ is a tunable, free parameter, to model the rapidity of the wind.

It is important to note here that this heuristic argument can be expected to break down for extreme initial conditions. For example, Boily & Kroupa (2003a) and Boily & Kroupa (2003b) have recently shown that the fraction of stars which remain bound after an impulsive mass loss is generally higher than standard virial arguments would suggest.

A1.2 Non-adiabatic inflow models

So far, we have considered only the special case of adiabatic gas inflow. We also present some simulations in which this assumption is relaxed. As such, it is instructive to attempt to consider analytically how we might expect the cusp contraction to change when gas is dropped on some shorter timescale, t_{cont} . To do this, it is helpful to consider the energy of a dark matter particle's orbit before and after the mass inflow. If we start with the same initial conditions before mass inflow as in section A1, then all of the particles start on circular orbits. Thus the initial specific energy, $E_{dm,i}$, of a dark matter particle at a radius, r , is given by:

$$E_{dm,i} = \frac{1}{2}v_{dm,i}(r)^2 + \Phi_{dm,i}(r) \quad (\text{A6})$$

where $v_{dm,i}(r)$ is the circular velocity of the particle at r and $\Phi_{dm,i}(r)$ is the local potential. After the mass infall, the local potential is increased by the addition of the baryons. For adiabatic changes, where circular orbits are maintained, this gives for the specific energy after mass infall, $E_{dm,f}^*$:

$$E_{dm,f}^* = \frac{1}{2}v_{dm,f}(r)^2 + \Phi_{dm,f}(r) + \Phi_b(r) \quad (\text{A7})$$

where the * denotes circular orbits, and $\Phi_b(r)$ is the baryonic contribution to the local potential.

Since angular momentum will be conserved throughout the mass inflow, circular orbits are then the lowest final energy state of the system. For more general initial conditions, one can think of the dark matter particles being *heated*. The adiabatic case, which preserves the initial orbital structure, is then the situation of *minimal heating*. Thus the adiabatic case produces the *lowest* final specific orbital energy for the dark matter after mass infall.

For non-adiabatic mass infall, the final specific energy of a dark matter particle, $E_{dm,f}$, will then be higher than for the adiabatic case:

$$E_{dm,f} = E_{dm,f}^* \delta_E \quad (\text{A8})$$

where $0 < \delta_E \leq 1$ essentially parameterises our ignorance about the final energy state of a dark matter particle. Notice that for $\delta_E = 1$ we recover circular orbits and adiabatic mass infall. For $\delta_E < 1$, the final energy state is *higher* in the sense that it is a smaller negative number, than for the adiabatic case. For non-adiabatic changes, some of the energy that would have gone into contracting the central dark matter cusp now goes into heating the central orbital structure. This produces *two* important effects: firstly, an initially isotropic velocity distribution for the dark matter will be heated and become more radially anisotropic in the centre. This is important since particles may then become more easily unbound after a subsequent mass loss. Secondly, the contraction of the halo can be expected to be less for non-adiabatic inflow than for the adiabatic case.

APPENDIX B: THE RESPONSE OF A STELLAR DISTRIBUTION TO IMPULSIVE GAS MASS LOSS

In this appendix we briefly summarise an analytic calculation to determine the response of the remaining baryons to an impulsive mass loss from the baryons. The approach is similar to the orbit integration method proposed by Schwarzschild (1979) for setting up equilibrium galaxies; however, the context is very different.

B1 Impulsive mass loss

We use initial conditions before mass loss as in section 2.1, but we place all of the baryon particles on randomly oriented circular orbits. For here on, ‘particle’ refers to a baryon or star particle.

In the impulsive regime, after the mass loss, particles which were initially on circular orbits with specific energy, E_i , at a radius, r_i , then move onto some more general orbit with specific energy, E_f , at a radius, $r_f(t)$, which is now a *function of time*. For general orbits in a spherically symmetric potential, it can be shown that $r_f(t)$ obeys the equation (Binney & Tremaine, 1987):

$$\left(\frac{dr_f}{dt}\right)^2 = 2(E_f - \Phi_f) - \frac{L^2}{r_f^2} \quad (\text{B1})$$

where $\Phi_f(r_f)$ is the potential of the baryons and dark matter after the mass loss and $L(r_i)$ is the angular momentum per unit mass of the orbit, which is fixed by angular momentum conservation to be the same as the angular momentum of the initial circular orbit at r_i .

Equation B1 has, for bound orbits, in general, two solutions where $\frac{dr_f}{dt} = 0$.

Thus, if $\Phi_f(r_f)$, $E_f(r_i)$ and $L^2(r_i)$ are known, we can calculate r_{max} and r_{min} from equation B1. We can then calculate the final density profile of the baryons, $\rho_{b,f}$, in the following way: rearranging equation B1, we can integrate to find the total time, t_{orb} , a particle spends moving from r_{min} to r_{max} . This gives:

$$t_{orb}(r_i) = \int_{r_{min}}^{r_{max}} \frac{dr_f}{\sqrt{2(E_f(r_i) - \Phi_f(r_f)) - \frac{L(r_i)^2}{r_f^2}}} \quad (\text{B2})$$

Furthermore, we can similarly calculate the time spent by the particle in some small, infinitesimal, radial slice between r and $r + dr$. This gives:

$$\begin{aligned} t_{slice}(r, r_i) &= \int_r^{r+dr} \frac{dr_f}{\sqrt{2(E_f(r_i) - \Phi_f(r_f)) - \frac{L(r_i)^2}{r_f^2}}} \\ &= dr \left(2(E_f(r_i) - \Phi_f(r_f)) - \frac{L(r_i)^2}{r^2} \right)^{-1} \end{aligned} \quad (\text{B3})$$

The *probability* of a particle initially at a radius, r_i , being at a radius, r , is then given by:

$$p(r, r_i) = \frac{t_{slice}(r, r_i)}{t_{orb}(r_i)} \quad (\text{B4})$$

So, to recapitulate: a particle initially at a radius, r_i , will move onto a time dependent orbit, $r_f(t)$, which samples a *range* of radii between r_{min} and r_{max} . The final mass distribution at some radius r of many particles will then be the statistical sum of the probabilities of finding each of the particles at r . Thus, if the initial density distribution of baryons is given by $\rho_{b,i}$, then the final density distribution will be given by:

$$4\pi r^2 \rho_{b,f}(r) dr = \int_0^\infty p(r, r_i) 4\pi r_i^2 \rho_{b,i}(r_i) dr_i \quad (\text{B5})$$

The term on the left hand side is in fact the final *mass* of an infinitesimal shell of radius, r and thickness, dr . However, this can be numerically differentiated to find the density profile and then numerically integrated to find the surface density profile.

The final potential after mass loss, $\Phi_f(r_f)$, may be calculated as in appendix A if it is assumed that the baryons contribute negligibly to the final potential. Thus, the only unknown in equation B3 is the final specific energy distribution of the baryon orbits, $E_f(r_i)$. In the adiabatic, or infinitely slow mass loss case, where the orbital structure is preserved, this may be simply calculated. In general, however, this value must be taken from the simulations.

APPENDIX C: VIOLENT RELAXATION IN A HERNQUIST POTENTIAL AND THE FORMATION OF EXPONENTIAL SURFACE DENSITY PROFILES

Lynden-Bell (1967) demonstrated that violent relaxation will cause particles to move towards a Maxwellian distribution (with temperature proportional to mass) irrespective of the initial conditions. Where relaxation ceases before equilibrium is reached; or where a

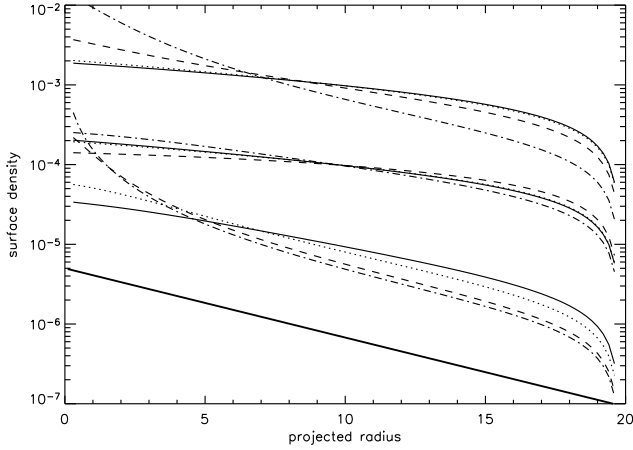


Figure C1. The surface density profile of a violently relaxed stellar population embedded in a Hernquist dark matter potential. The curves have been offset from one another for clarity. From top to bottom the three sets of curves show: 1. the effect of varying β for a fixed halo potential (the solid, dotted, dashed and dot-dashed lines are for $\beta = 0.1, 1, 5$ and 10 respectively); 2. the effect of varying the halo potential for fixed β (the lines are for halos with the same initial conditions as models B1-B4 (see table 1) and 3. the effect of varying the velocity anisotropy parameter, r_a (the lines are for $r_a = 10, 5, 1$ and 0.1 respectively). A true exponential surface density is also marked for comparison (thick solid line at the bottom).

non-Maxwellian steady state solution is reached first, the system should still be close to Maxwellian (Lynden-Bell, 1967). Furthermore the system is more likely to achieve isotropy at small radii, where dynamical times are short, than at larger radii. As such, we follow Osipkov (1979) and Merritt (1985) and parameterise the final post-mass loss non-isotropic baryon distribution function by the following form:

$$f = Ae^{-\beta(E+L^2/2r_a^2)} \quad (\text{C1})$$

where E is the specific energy of the baryons, L is the specific angular momentum and r_a is the radius at which the velocity of the baryons moves from being isotropic to being anisotropic (Osipkov (1979) and Merritt (1985)). Notice that for $r_a \rightarrow \infty$ we recover the true Maxwellian distribution at all radii.

The density of the baryons after mass loss may then be calculated from f as in Binney & Tremaine (1987) to give:

$$\rho(\psi, r) = \frac{2\sqrt{2\pi}A(\sqrt{\pi}e^{\beta\psi}\text{erf}(\sqrt{\beta\psi}) - 2\sqrt{\beta\psi})}{\beta^{3/2}(1 + (r/r_a)^2)} \quad (\text{C2})$$

and final surface density numerically integrated from the above equation using the effective potential, ψ , for a generalised Hernquist profile (see equation 2 and Binney & Tremaine (1987) for a definition of the effective potential).

Figure C1 shows the surface density profiles calculated as above for a wide range of halo potential parameters, and values of β and r_a (while β should strictly be calculated from the total energy of the system, we treat this here as a free parameter).

Notice that only two of the curves deviate strongly from an exponential near the centre: the dashed and dot-dashed lines in the bottom set of curves. These two curves were for $r_a = 1$ and 0.1 respectively. In both cases this represents a much more significant central velocity anisotropy than was observed in any of the simulations presented in this paper. As mentioned above, it should be of

no surprise than the baryons achieve approximate isotropy at small radii where the dynamical times are short: the system relaxes fully at these radii into a Maxwellian distribution.